Deep slab collision during Miocene subduction causes uplift along crustal-scale reverse faults in Fiordland, New Zealand

Keith Klepeis[1], Laura Webb[1], Hannah Blatchford[1*], Joshua Schwartz[2], Richard Jongens[3], Rose Turnbull[4], Harold Stowell[5]

[1]*Dept. of Geology, 180 Colchester Ave., University of Vermont, Burlington, VT, 05405 USA*

[2]*Dept. of Geological Sciences, California State University Northridge, 18111 Nordhoff St., Northridge, CA 91330 USA*

[3]*Anatoki Geoscience Ltd, 64 Skibo St., Dunedin, 9012, New Zealand*

[4]*GNS Science, Dunedin Research Centre, Private Bag 1930, Dunedin, 9054, New Zealand*

[5]*Dept. of Geological Sciences, University of Alabama, 2003 Bevill Bldg., Tuscaloosa, AL 35487 USA*

[*]*now at Dept. of Earth Sciences, University of Minnesota,116 Church St., Minneapolis, MN 55455 USA*

ABSTRACT

A new multidisciplinary project in southwest New Zealand that combines geological and geophysical data shows how and why deep lithospheric displacements were transferred vertically through the upper plate of an incipient ocean-continent subduction zone. A key discovery includes two zones of steep, downward-curving reverse faults that uplifted and imbricated large slices of Cretaceous lower, middle, and upper crust in the Late Miocene. Geochemical and structural analyses combined with $^{40}Ar/^{39}Ar$ geochronology and published images from seismic tomography suggest that the reverse faults formed at 8–7 Ma as a consequence of a deep (~100 km) collision between subducting oceanic lithosphere and previously subducted material. This collision localized shortening and reactivated two crustal-scale shear zones from the upper

mantle to the Earth's surface. The event, which is summarized in a new lithospheric-scale profile, is helping us answer some long-standing questions about the origin of Fiordland's unique lower-crustal exposures and what they tell us about how inherited structures can transfer motion vertically through the lithosphere as subduction initiates.

INTRODUCTION

In southwest New Zealand, oceanic lithosphere of the Australian Plate subducts obliquely beneath continental lithosphere of the Pacific Plate at the Puysegur Trench (Fig. 1A). Northeast of the trench, the subducted slab rotates and steepens to vertical below Fiordland where it joins the Alpine Fault (Reyners et al., 2017), a ~850 km transform that has accumulated some 480 km of horizontal displacement since ~25 Ma (Sutherland and Norris, 1995). This region has generated great interest among geologists, in part because it is one of only a few places where the surface tectonic record of an incipient ocean-continent subduction zone can be observed directly (Mao et al., 2017). It also represents Earth's deepest exposed example of an Andean-style continental arc (Ducea et al., 2015). Here, we use this unique setting to explore how Fiordland's surface and crust responded to events that occurred deep within the lithospheric mantle since subduction began in the early Miocene.

Over the past few years, our understanding of the vertical links that develop within the lithosphere has benefitted from improvements in our ability to extract information from the rock record. Innovative approaches to studying fault zones that combine geochemistry and high-precision geochronology with structural analyses, for example, have enhanced our capacity to relate deformation histories to other processes across a wide range of scales (e.g., Haines et al., 2016; Schwartz et al., 2016; Williams et al., 2017). At the same time, new methods in global teleseismic tomography are revealing the geometry and extent of material that was subducted into the mantle millions of years ago in unprecedented detail (Wu et al., 2016; Reyners et al., 2017). These imaged slabs can be integrated with surface geology and plate kinematics to reveal previously hidden tectonic histories. Together these and many other innovations are providing new opportunities to determine how surface tectonic records connect to processes occurring in the mantle as subduction zones form and develop over time (e.g., Liu, 2015; Liu et al., 2017; Kissling and Schlunegger, 2018).

In this article, we integrate structural, geochemical, and geochronologic data with images of the upper mantle derived from seismic tomography to reconstruct the late Cenozoic tectonic history of Fiordland. The results provide new insights into the process of subduction initiation at continental margins, including the causes and consequences of vertical motions within the overriding plate.

PREVIOUS WORK

Surface geology

The surficial geology of Fiordland is dominated by exposures of the Median Batholith (Mortimer et al., 1999), which consist mostly of Carboniferous–Early Cretaceous plutons. An eastern (outboard) belt contains Jurassic and older rocks that accreted onto the Gondwana margin during the Early Cretaceous (Tulloch and Kimbrough, 2003; Marcotte et al., 2005). A western (inboard) belt exposes the Early Cretaceous Western Fiordland Orthogneiss (WFO), which was emplaced mainly as diorite into Paleozoic plutonic and metasedimentary rocks at the base of a Mesozoic arc (Bradshaw, 1990). Early petrologic investigations showed that the western belt records high metamorphic temperatures ($T \geq 750°C$) and a depth of exposure that is unique in New Zealand (Oliver, 1976; Blattner, 1976; Bradshaw, 1985). Approximately 35% of the WFO contains high-P mineral assemblages indicative of garnet granulite, omphacite granulite, and eclogite facies metamorphism (Turnbull et al., 2010), making it Earth's largest (~4500 km^2) and deepest (to at least 65 km) known exposure of lower crust from a Mesozoic continental arc (Ducea et al., 2015).

Rock uplift and topographic growth

Sutherland et al. (2009) documented the onset of rapid exhumation in SW Fiordland at 25–15 Ma, coincident with the initiation of subduction south of New Zealand. During the 15–5 Ma period, zones of high exhumation rates broadened and expanded into the interior of Fiordland, although exhumation occurred mainly in the west. These patterns, which include an estimated 12–15 km of total rock uplift, are thought to be associated with the development of elevated topography. They also have been interpreted to result from either a combination of crustal shortening and dynamic uplift above the subducting slab (Sutherland et al., 2009) and/or glacial erosion coupled with high (>8 m/ yr^{-1}) precipitation rates (Jiao et al., 2017). Although Sutherland et al. (2009) postulated that age-elevation relationships and spatial variations in exhumation rates were caused by reverse faulting, their relationship to specific faults was unresolvable with existing data.

Subsurface imaging

A regional 3-D seismic velocity model derived from seismic tomography studies by Eberhart-Phillips et al. (2010) has recently allowed geophysicists to image the subsurface extent of the partially subducted Hikurangi Plateau beneath New Zealand (Fig. 1, inset) (Reyners et al., 2011; Davy, 2014). This oceanic plateau formed at ~122 Ma (Neal et al., 1997) and was underthrust beneath the continent twice. The first underthrusting occurred at ~100 Ma when Fiordland formed part of Gondwana, the second occurred in the late Cenozoic driven by convergence between the Pacific and Australian plates (Davy, 2014; Reyners et al., 2011; 2017).

Currently, the western edge of the plateau lies below central and northern Fiordland where it impacts the geometry of subducting Australian Plate (Reyners et al., 2017). South of the line of section shown in Fig. 1A, the subducting plate parallels the Puysegur Trench and dips at ~68° below 50 km depth (Reyners et al., 2011). North of this line, the slab twists to the NE (040°) and is vertical below 75 km (Reyners et al., 2017).

INTEGRATED GEOLOGICAL STUDIES

Reconstructing Fiordland

Many advances in our understanding of Fiordland’s deep-crustal exposures have come from efforts to distinguish the age and significance of various episodes of magmatism, metamorphism, and deformation. In particular, the application of multiple geochronometers (e.g., Klepeis et al., 2016; Schwartz et al., 2016; 2017; Stowell et al., 2017; Tulloch et al., 2010; 2019), combined with an improved understanding of metastability in igneous and metamorphic mineral assemblages (Allibone et al., 2009a; Bhattacharya et al., 2018), have enhanced our ability to correlate tectonic events across thousands of square kilometers. These improvements have allowed us to reconstruct Fiordland's crustal architecture with increased accuracy.

Figure 1A shows a new compilation of Cretaceous paleodepths that provides a snapshot of Fiordland crust at ~115 Ma, when it reached its maximum thickness of ≥65 km. It also is the first to delineate the boundaries of the various crustal blocks. The data derive from mineral assemblages that represent the peak of Early Cretaceous metamorphism and estimates of the emplacement depths of plutons whose age and history are known (Table 1, Supplementary Material). Our reconstruction shows large blocks of Cretaceous upper, middle, and lower crust, all of which are bounded by faults. These crustal divisions are important because they provide an improved framework for determining how the characteristics of magmatism, metamorphism, and deformation change vertically within the lithosphere.

One of the most significant outcomes of our study is the discovery of a narrow zone of steep, downward-curving reverse faults that placed a large, irregular slice of lower crust up and to the east over the middle and upper crust (Figs. 1A, 2A). The Spey-Mica Burn (SM) fault system, which is well-exposed in central Fiordland, extends for ~80 km and joins the Misty Fault (new name) along the eastern boundary of the lower crustal block. The fault zone then steps to the east in a series of oblique-slip faults that connect with another system of reverse faults, including the Mt Thunder Fault (new name) and the Glade-Darran fault zone (Fig. 1, Table 2 in Supplementary Material). This discovery is the first to confirm that the last 12–15 km of the uplift and exhumation of Fiordland's unique exposures is directly related to late Cenozoic reverse faulting rather than to an older period of Cretaceous extension. Consequently, it has sparked new investigations aimed at determining the age of faulting and its relationship to Miocene subduction and zones of high exhumation rates.

Reactivating ancient structures

Determining the age and history of faulting in Fiordland has been challenging, mainly because the surface expression of faults typically is narrow and eroded, or concealed by sediment and dense vegetation. To solve this problem, we walked the surface traces of faults and found high-quality exposures that preserve kinematic information. Two especially informative localities (stars in Fig. 1B) expose pseudotachylyte-bearing reverse faults at and near the eastern boundary of the lower crustal block. These sites show that the reverse faults reactivated two ancient crustal boundaries that coincide with large, ductile shear zones. The western boundary, which is centered on the George Sound shear zone, is marked in part by a linear belt of Late

Carboniferous granites (Ramezani and Tulloch, 2009) within the lower crustal block (Fig. 1B). The eastern boundary coincides with the old Carboniferous edge of Gondwana (Marcotte et al., 2005; Allibone et al., 2009b; Scott et al., 2011; McCoy-West et al., 2014) and is deformed by both the Grebe and the Indecision Creek shear zones (Fig. 1B). All of these structures were infiltrated by magma and reactivated multiple times since the late Carboniferous, (e.g. Marcotte et al., 2005; Scott et al., 2011) (Fig. 1B), indicating that they represent long-lived zones of crustal weakness.

Figure 2A provides a detailed view of the superposed deformations caused by the repeated reactivation of the western boundary. It shows the Carboniferous Cozette pluton (pink) was intruded by the Early Cretaceous (mainly 118–115 Ma) Misty pluton (yellow), both of which are deformed by the George Sound shear zone (red-lined pattern). This same zone also was the site of repeated magma infiltration during the 170–128 Ma interval (blue) (Allibone et al., 2009b). Two phases of steep reverse faulting then imbricated the shear zone, placing lower crust to the east over middle crust.

These findings have allowed us to formulate many new questions, such as: How old is the crustal imbrication? Why do faults deform only parts of the Late Carboniferous boundaries? Our collaborative study aims to answer these questions and, in doing so, determine how the Paleozoic–Mesozoic history of Gondwana influenced Fiordland's late Cenozoic tectonic history.

Unraveling the timing of fault reactivations

An especially useful approach to distinguishing the age of superposed events at the boundaries of Fiordland's lower crustal slice has been through the use of $^{40}Ar/^{39}Ar$ age spectra derived from step-heating experiments. For example, hornblende from the George Sound shear zone where it deforms the Carboniferous Cozette pluton (sample 79, Fig. 2B) yields a 116.1 ±

1.1 Ma (1σ) plateau age after an initial complex release pattern. A second sample from where the shear zone deforms this sample pluton (sample 72, Fig. 2B) yielded similar hornblende spectra and a 111.14 ± 0.76 Ma biotite plateau age. These ages help establish that Cretaceous magmatism and transpression overlapped in space and time, with pluton emplacement occurring mainly at 118–115 Ma (Schwartz et al., 2016) and the deformation occurring at 117–110 Ma (Fig. 2B). They also help establish this zone as a long-lived boundary that was in place prior to subduction initiation at the Puysegur Trench during the Miocene.

To determine the age of the reverse faults, we collected two samples of pseudotachylyte from a well-exposed segment of the Spey-Mica Burn fault zone (samples 22, 23, Fig. 2A) and a third pseudotachylyte sample (3A) from the Mt. Thunder Fault (location in Fig. 1B, results shown in Supplementary Material). Multiple runs of all three samples helped us cross check the reproducibility of the apparent age spectra and interpreted ages. The results indicate that the pseudotachylytes all range in age from 8–7 Ma, indicating that faulting occurred approximately simultaneously within both fault zones.

Probing the deep roots of faults

One of the outcomes of the crustal configuration shown in Figures 1A and 1B is an improved framework for determining how structures and tectonic processes are expressed at different depths within the lithosphere. For example, our work shows that it is possible to walk continuously along the boundary between the Paleozoic Gondwana margin and the outboard Jurassic arc from its location in upper crustal exposures at the southern end of the Grebe shear zone to its lower crustal expression in the Indecision Creek shear zone (Fig. 1B). This physical relationship shows how narrow zones of Cretaceous faulting in the upper crust gradually change into thick zones of ductile shear in the lower crust (Fig. 1B). In addition, the systematic mapping and dating of plutons along the length of the shear zones shows that magmatism and deformation were synchronous within them at all levels of the crust (Marcotte et al., 2005; Klepeis et al., 2016; Schwartz et al., 2017). This close association is important because it allows us to use the geochemical signatures and source regions of plutons to determine how deep the George Sound and Indecision Creek shear zones once penetrated.

Over the last few years, several studies (Decker et al., 2017; Milan et al., 2017) have investigated the deep source regions of the WFO batholith using isotopic systems and geochemical data. Decker et al. (2017) showed that Early Cretaceous plutons emplaced into the crustal boundary marked by the George Sound shear zone (Figs. 1B, 2, 3) were sourced below the continental crust. Structural studies indicate that deformation aided magma ascent (Betka and Klepeis, 2013; Klepeis et al., 2016). Further work using oxygen and hafnium isotopes (Andico et al., 2017) indicates that strong isotopic differences in the lower crust existed across these shear zones during the Jurassic and Cretaceous, indicating they extended to lower crustal depths during, and prior to, these times. This work is important for understanding Fiordland's current crustal architecture because it implies that the Spey-Mica Burn fault system, which reactivated two ancient crustal-scale shear zones in the Late Miocene, also transects the crust and penetrates into the upper mantle.

CONNECTING SURFACE GEOLOGY TO DEEP LITHOSPHERIC STRUCTURES

Our ability to investigate vertical connections between Fiordland's surface and the deep lithosphere requires a detailed knowledge of crustal architecture, including when and how it was assembled. Figure 3 shows a new profile that combines information from Fiordland's rock record with recently published tomographic models of the deep crust and upper mantle (Eberhart-Phillips et al., 2010; Reyners et al., 2017). The profile shows two narrow zones of reverse faulting directly above the region where the subducting Australian Plate steepens to vertical against the Hikurangi Plateau. This discovery not only enhances our ability to reconstruct Fiordland's subduction history, it also suggests a new mechanism by which Fiordland's crustal architecture and surface record are linked to processes occurring at the base of the lithosphere.

Estimates of crustal thickness beneath Fiordland, derived from isovelocity plots of Vp=7.5 km s^{-1} (Eberhart-Phillips et al., 2010; Reyners et al., 2017), suggest that Moho depths vary from about 30 km below the WFO to more than 50 km below the outboard batholith (Fig. 3). These estimates closely match those we obtained for Cretaceous crustal thicknesses using metamorphic mineral assemblages combined with estimates of the vertical offset across faults. This similarity suggests that the Cretaceous Moho approximately coincides with the position of the current Moho, which has been difficult to image using geophysical techniques. It also suggests that the apparent shallowing of both the Cretaceous and the current Moho from east to west beneath Fiordland is a consequence of Late Miocene reverse faulting. This interpretation is compatible with the steep orientation of the reverse faults, their reactivation of inherited crustal-scale shear zones, and estimates of 12–15 km of late Cenozoic uplift within their hanging walls.

Below the base of the crust, tomographic images show the 3-D structure and subsurface extent of the subducted Hikurangi Plateau (Reyners et al., 2011; Davy, 2014; Reyners et al., 2017). Images of Vp and Vp/Vs show that the plateau within the Pacific Plate mantle is a ~35 km thick zone of seismicity with a layer of high Vp (~8.5 km s^{-1}) eclogite crust at its base (Fig. 3). Above this layer, high Vp/Vs ratios (~1.75) probably reflect the presence of a hydrated mantle wedge, which may contribute to the poorly defined Moho. The plateau's southwest edge lies below central and northern Fiordland where it appears to step to the northeast. Interestingly, the pattern of Miocene reverse faults at the surface mimics this east-stepping geometry of the plateau at depth (Fig. 1B), which provides an explanation for why the two ancient crustal boundaries were reactivated in different places at 8–7 Ma.

In their tomographic studies of the subsurface, Reyners et al. (2011; 2017) concluded that a late Cenozoic collision between the subducting Australian Plate and the western Hikurangi Plateau caused the underthrust plate to steepen to vertical below 75 km (Fig. 3). A reconstruction of the forward progress of this slab since ~25 Ma (Fig. 1A) shows that the time when its leading edge first encountered the plateau margin coincides with both the surface location and the timing of reverse faulting at 8–7 Ma. This relationship suggests that the collision localized shortening and caused the reactivation of two Cretaceous shear zones as reverse faults. Their steep orientations meant that the displacements were partitioned mostly into vertical motion, suggesting that this event also should be visible in Fiordland’s exhumation history.

In their compilation of Fiordland’s record of surface uplift, Sutherland et al. (2009) inferred that topographic growth and exhumation since ~25 Ma were associated with the inception of subduction and the downward deflection of the Australian slab. However, one problem in trying to relate this history of uplift and exhumation to crustal shortening is that neither topographic features nor zones of high exhumation rates could be linked to specific faults. Our discovery of major reverse faults at the edge of Fiordland’s lower crustal block helps to solve this problem. In particular, the close spatial and temporal agreement between vertical fault motions at 7–8 Ma and the abrupt expansion of zones of rock uplift and high exhumation rates into eastern and northern Fiordland suggests that these uplift patterns were caused by reverse faulting. We therefore conclude that fault-related uplift and topographic growth in the late Miocene were direct consequences of the collision between the subducting Australian Plate and the Hikurangi Plateau.

CONCLUSIONS

The integration of surface and subsurface data sets from southwest New Zealand shows how the history of deformation, exhumation, and fault-related topographic growth above a young ocean-continent subduction zone is linked to events occurring near the base of the continental lithosphere. New geologic mapping and $^{40}Ar/^{39}Ar$ dates show that crustal-scale reverse faults reactivated two ancient shear zones at 8–7 Ma, placing an irregular slice of Cretaceous lower crust up and to the east over the middle and upper crust. The size, age, location, and style of these faults suggest that they formed as a direct consequence of a Late Miocene collision between the leading edge of the subducting Australian Plate and previously subducted oceanic crust of the Cretaceous Hikurangi Plateau. This collision, which occurred at ~100 km depth, localized shortening and caused the subducting slab to steepen to vertical. It also drove the reactivation of inherited structures, resulting in crustal imbrication and 12–15 km of vertical uplift. Integrated structural and geochemical analyses suggest that the reverse faults penetrate the entire crust and offset the Moho. The irregular geometry of the Hikurangi Plateau at depth provides a plausible explanation for why two ancient shear zones were reactivated simultaneously in different places at 8–7 Ma. For the first time, this study shows when, how, and why Earth's largest and deepest known exposure of lower crust from a Mesozoic continental arc was uplifted, imbricated, and exhumed to the surface above the Puysegur subduction zone. It also illustrates how inherited zones of crustal weakness facilitate the transfer of displacements between the Earth's surface and the upper mantle during the early stages of subduction.

SUPPLEMENTARY MATERIALS

This paper has an appendix.

ACKNOWLEDGMENTS

Financial support was provided by NSF grant EAR-1119248. We thank A. Tulloch and N. Mortimer at GNS (Dunedin) for discussions and assistance. D. Jones (Vermont) provided expertise and assistance with the argon analyses. We thank the Dept. of Conservation Te Anau office for access and permission to sample and two anonymous reviewers for helping to improve the manuscript.

REFERENCES CITED

Allibone, A.H., Milan, L.A., Daczko, N.R., and Turnbull, I.M., 2009a, Granulite facies thermal aureoles and metastable amphibolite facies assemblages adjacent to the Western Fiordland Orthogneiss in southwest Fiordland, New Zealand: Journal of Metamorphic Geology, v. 27, p. 349-369.

Allibone, A.H., Jongens, R., Turnbull, I.M., Milan, L.A., Daczko, N.R., De Paoli, M.C., and Tulloch, A.J., 2009b, Plutonic rocks of western Fiordland, New Zealand: field relations, geochemistry, correlation, and nomenclature: New Zealand Journal of Geology and Geophysics, v. 52, p. 379-415.

Andico, S., Schwartz, J.J., Tulloch, A. Turnbull, R., Klepeis, K., Miranda, E.A., Kitajima, K., and Ringwood, M.F., 2017, Oxygen Isotope Mapping Reveals a Crustal-Scale Structure within the Median Batholith, Fiordland, New Zealand: Geological Society of America Abstracts with Programs, v. 49, no. 6, doi: 10.1130/abs/2017AM-305151.

Betka, P.M., and Klepeis, K.A., 2013, Three-stage evolution of lower crustal gneiss domes at Breaksea Entrance, Fiordland, New Zealand: Tectonics, v. 32, p. 1084–110.

Bhattacharya, S., Kemp, A. I. S., Collins, W.J., 2018, Response of zircon to melting and metamorphism in deep arc crust, Fiordland (New Zealand): implications for zircon inheritance in cordilleran granites: Contributions to Mineralogy and Petrology, v. 173, no. 28, p. 1-36.

Blattner, P., 1976, Replacement of hornblende by garnet in granulite facies assemblages near Milford Sound, New Zealand: Contributions to Mineralogy and Petrology, v. 55, p. 181–190.

Bradshaw, J.Y., 1985, Geology of the northern Franklin Mountains, northern Fiordland, New Zealand, with emphasis on the origin and evolution of Fiordland granulites [Ph.D. thesis]: Dunedin, New Zealand, University of Otago, 379 p.

Bradshaw, J.Y., 1990, Geology of crystalline rocks of northern Fiordland; details of the granulite facies western Fiordland Orthogneiss and associated rock units: New Zealand Journal of Geology and Geophysics, v. 33, p. 465-484.

Davy, B., 2014, Rotation and offset of the Gondwana convergent margin in the New Zealand region following Cretaceous jamming of Hikurangi Plateau large igneous province subduction: Tectonics, v. 33, p. 1577–1595.

Decker, M., Schwartz, J.J., Stowell, H.H., Klepeis, K.A., Tulloch, A.J., Kitajima, K., Valley, J.W., Kylander-Clark, A.R.C., 2017, Slab-Triggered Arc Flare-up in the Cretaceous Median Batholith and the Growth of Lower Arc Crust, Fiordland, New Zealand: Journal of Petrology, v. 58, no. 6, p. 1145-1171.

Ducea, M.N., Saleeby, J.B., and Bergantz, G., 2015, The Architecture, Chemistry, and Evolution of Continental Magmatic Arcs: Annual Reviews of Earth and Planetary Science, v. 43, p. 10.1–10.33.

Eberhart-Phillips, D., Reyners, M., Bannister, S., Chadwick, M., and Ellis, S., 2010, Establishing a versatile 3-D seismic velocity model for New Zealand: Seismological Research Letters, v. 81, no. 6, p. 992–1000.

Haines, S., Lynch, E., Mulch, A., Valley, J.W., and Pluijm, B.V.D., 2016, Meteoric fluid infiltration in crustal-scale normal fault systems as indicated by $\delta^{18}O$ and $\delta^{2}H$ geochemistry and $^{40}Ar/^{39}Ar$ dating of neoformed clays in brittle fault rocks: *Lithosphere*, v. 8, p. 587–600.

Jiao, R., Herman, F., and Seward, D., 2017, Late Cenozoic exhumation model of New Zealand: Impacts from tectonics and climate: Earth-Science Reviews, v. 166, p. 286-298.

Kissling, E., and Schlunegger, F., 2018, Rollback orogeny model for the evolution of the Swiss Alps: Tectonics, v. 37, p. 1097–1115.

Klepeis, K.A., Schwartz, J., Stowell, H., and Tulloch, A., 2016, Gneiss domes, vertical and horizontal mass transfer, and the initiation of extension in the hot lower crustal root of a continental arc, Fiordland, New Zealand: Lithosphere, v. 8, p. 116–140.

Liu, S., Gurnis, M., Ma, P., and Zhang, B., 2017, Reconstruction of northeast Asian deformation integrated with western Pacific plate subduction since 200 Ma: Earth-Science Reviews, v. 175, p. 114–142.

Liu, L., 2015, The ups and downs of North America: Evaluating the role of mantle dynamic topography since the Mesozoic: Reviews of Geophysics, v. 53, p. 1022–1049.

Mao, X., Gurnis, M., and May, D.A., 2017, Subduction initiation with vertical lithospheric heterogeneities and new fault formation: Geophysical Research Letters, v. 44, p. 11,349–11,356.

Marcotte, S.B., Klepeis, K.A., Clarke, G.L., Gehrels, G., and Hollis, J.A., 2005, Intra-arc transpression in the lower crust and its relationship to magmatism in a Mesozoic magmatic arc: Tectonophysics, v. 407, p. 135-163.

McCoy-West J., Mortimer, N., and Ireland, T.R., 2014, U–Pb geochronology of Permian plutonic rocks, Longwood Range, New Zealand: implications for Median Batholith–Brook Street Terrane relations: New Zealand Journal of Geology and Geophysics, v. 57, no. 1, p. 65-85.

Milan, L.A., Daczko, N.R., and Clarke, G.L., 2017, Cordillera Zealandia: A Mesozoic arc flare-up on the palaeo-Pacific Gondwana Margin: Scientific Reports, v. 7, no. 1, p. 261.

Mortimer, N., Tulloch, A.J., Spark, R.N., Walker, N.W., Ladley, E., Allibone, A., and Kimbrough, D.L., 1999, Overview of the Median Batholith, New Zealand: a new interpretation of the geology of the Median Tectonic Zone and adjacent rocks: Journal of African Earth Sciences, v. 29, p. 257-268.

Neal, C.R., Mahoney, J.J., Kroenke, L.W., Duncan, R.A., Petterson, M.G., 1997, The On- tong Java Plateau: Geophysical Monograph, v. 100, p. 183–216.

Oliver, G.J.H., 1976, High grade metamorphic rocks of Doubtful Sound, Fiordland, New Zealand: A study of the lower crust [Ph.D. thesis]: Dunedin, New Zealand, University of Otago, 547 p.

Ramezani, J., and Tulloch, A.J., 2009, TIMS U-Pb geochronology of southern and eastern Fiordland: http://data.gns.cri.nz/paperdata/index.jsp, doi: 10.21420/G2CC7Z.

Reyners, M., Eberhart-Phillips, D., Bannister, S., 2011, Tracking repeated subduction of the Hikurangi Plateau beneath New Zealand: Earth and Planetary Science Letters, v. 311, p. 165-171.

Reyners, M., Eberhart-Philips, D., Upton, P., and Gubbins, D., 2017, Three-dimensional imaging of impact of a large igneous province with a sub- duction zone, Earth and Planetary Science Letters, v. 460, p. 143–151.

Schwartz, J.J., Stowell, H.H., Klepeis, K.A., Tulloch, A.J., Kylander-Clark, A.R.C., Hacker, B.R., and Coble, M.A., 2016, Thermochronology of extensional orogenic collapse in the deep crust of Zealandia: Geosphere, v. 12, p. 647–677.

Schwartz, J.J., Klepeis, K.A., Sadorski, J.F., Stowell, H.H., Tulloch, A.J., and Coble, M.A., 2017, The tempo of continental arc construction in the Mesozoic Median Batholith, Fiordland, New Zealand: Lithosphere, v. 9, no. 3, p. 343-365.

Scott, J.M., Cooper, A.F., Tulloch, A.J., and Spell, T.L., 2011, Crustal thickening of the Early Cretaceous paleo-Pacific Gondwana margin: Gondwana Research, v. 20, p. 380-394.

Stowell, Harold H., J.J. Schwartz, K.A. Klepeis, C. Hout, A.J. Tulloch, A. Koenig, 2017, Sm-Nd garnet ages for granulite and eclogite in the Breaksea Orthogneiss and widespread granulite facies metamorphism of the lower crust, Fiordland magmatic arc, New Zealand: Lithosphere, v. 9, no. 6, p. 953-975.

Sutherland, R., and Norris, R.J., 1995, Late Quaternary displacement rate, paleoseismicity, and geomorphic evolution of the Alpine Fault: evidence from Hokuri Creek, South Westland, New Zealand: New Zealand Journal of Geology and Geophysics, v. 38, p. 419–430.

Sutherland, R., Gurnis, M., Kamp, P.J.J., and House, M.A., 2009, Regional exhumation history of brittle crust during subduction initiation, Fiordland, southwest New Zealand, and implications for thermochronologic sampling and analysis strategies: Geosphere, v. 5, no. 5, p. 409-425.

Tulloch, A.J., and Kimbrough, D.L., 2003, Paired plutonic belts in convergent margins and the development of high Sr/Y magmatism: Peninsular Ranges batholith of Baja-California and Median batholith of New Zealand, *in* Johnson, S.E., Paterson, S.R., Fletcher, J.M., Girty, G.H., Kimbrough, D.L., and Martín-Barajas, A., eds., Tectonic evolution of northwestern México and the southwestern USA: Boulder, Colorado, Geological Society of America Special Paper 374, p. 275–295.

Tulloch, A.J., Ireland, T.R., Kimbrough, D.L., Griffin, W.L., and Ramezani, J., 2010, Autochthonous inheritance of zircon through Cretaceous partial melting of Carboniferous plutons: The Arthur River Complex, Fiordland, New Zealand: Contributions to Mineralogy and Petrology, v. 161, p. 401–421.

Turnbull, I.M., Allibone, A.H., and Jongens, R., 2010, Geology of the Fiordland area: Institute of Geological and Nuclear Sciences, Lower Hutt, New Zealand, scale 1:250 000, sheet 17, 97 p. text.

Tulloch, A.J., Mortimer, N., Ireland, T.R., Waight, T.E., Maas, R., Palin, J. M., et al., 2019, Reconnaissance basement geology and tectonics of South Zealandia: Tectonics, v. 38. https://doi.org/10.1029/2018TC005116

Williams, R.T., Goodwin, L.B., Sharp, W.D., and Mozley, P.S., 2017, Reading a 400,000-year record of earthquake frequency for an intraplate fault: Proceedings of the National Academy of Sciences of the United States of America, v. 114, p. 4893–4898.

Wu, J., Suppe, J., Lu, R., and Kanda, R., 2016, Philippine Sea and East Asian plate tectonics since 52 Ma constrained by new subducted slab reconstruction methods: Journal of Geophysical Research: Solid Earth, v. 121, p. 4670–4741.

FIGURE CAPTIONS

Figure 1. (A) Map of Fiordland showing the imbrication of Cretaceous lower, middle and upper crust by Miocene reverse faults. Profile along line of section A-A' is shown in Figure 2. Paleodepth uncertainties are ±0.1 GPa (±3.7 km). Reconstruction of the subducting Australian Plate at 20, 12, and 7 Ma is from Sutherland et al. (2009). AF-Alpine Fault, GD-Glade-Darran fault zone, HP-Hikurangi Plateau, HT-Hikurangi Trench, M-Misty Fault, MT-Mt. Thunder Fault, SM-Spey-Mica Burn fault zone. (B) Map showing position of two Carboniferous crustal boundaries (black dashed lines). The western boundary coincides with the George Sound shear zone (GSSZ) and SM fault zone. The eastern one coincides with the Grebe and Indecision Creek (ISCZ) shear zones, and Mt Thunder Fault. WFO is Western Fiordland Orthogneiss. Location of three pseudotachylyte samples (22, 23, 3A) dated at 8–7 Ma are shown with white stars. Dashed black line surrounding light blue region represents high Vp (~8.5 km s^{-1}) eclogite crust at the base of the Hikurangi Plateau at ~100 km depth (after Reyners et al., 2017).

Figure 2. (A) Cross section of the Spey-Mica Burn fault zone (location in Fig. 1B). Profile shows steep reverse faults (dark black lines) that uplifted and imbricated the George Sound shear zone (red-lined pattern), placing Cretaceous lower crust to the SE over Cretaceous middle crust. Yellow and blue represent undeformed portions of the Misty pluton and older Jurassic-Early Cretaceous igneous rock, respectively. Light red-lined pattern represents sheared Misty pluton, dark red-lined pattern with plusses represents sheared Cozette pluton (samples 72 and 79). (B) Apparent $^{40}Ar/^{39}Ar$ age spectra from hornblende (hbl) and biotite (bt) from sample 72 and hornblende from sample 79 indicate George Sound shear zone (GSSZ) deformation occurred at 117–110 Ma (dots are dated samples). (C) Apparent $^{40}Ar/^{39}Ar$ age spectra from 8–7 Ma pseudotachylyte (psd) within splays of the Spey-Mica Burn fault zone (two runs each of samples 22 and 23). Similar ages were obtained from pseudotachylyte in the Mt Thunder Fault

(Fig. 2 and 3 in Supplementary Material shows detailed spectra and a detailed map of the fault zone, respectively).

Figure 3. Vertical profile that combines new geological information with published geophysical images (location in Fig. 1). Colors match those in Fig. 1A except where noted. The location and geometry of the subducted Australian Plate is from relocated hypocenters (Reyners et al., 2017). The location of the subducted Hikurangi Plateau is from Eberhart-Phillips et al. (2010) and Reyners et al. (2017). Grey lines are Cretaceous shear zones that penetrate the lower crust: G-George Sound shear zone, I-Indecision Creek shear zone, Gr-Grebe shear zone.

[11]GSA Data Repository item 201Xxxx, $^{40}Ar/^{39}Ar$ analytical methods and data tables, paleodepth data, and fault-slip data are available online at www.geosociety.org/pubs/ft20XX.htm, or on request from editing@geosociety.org or Documents Secretary, GSA, P.O. Box 9140, Boulder, CO 80301, USA.

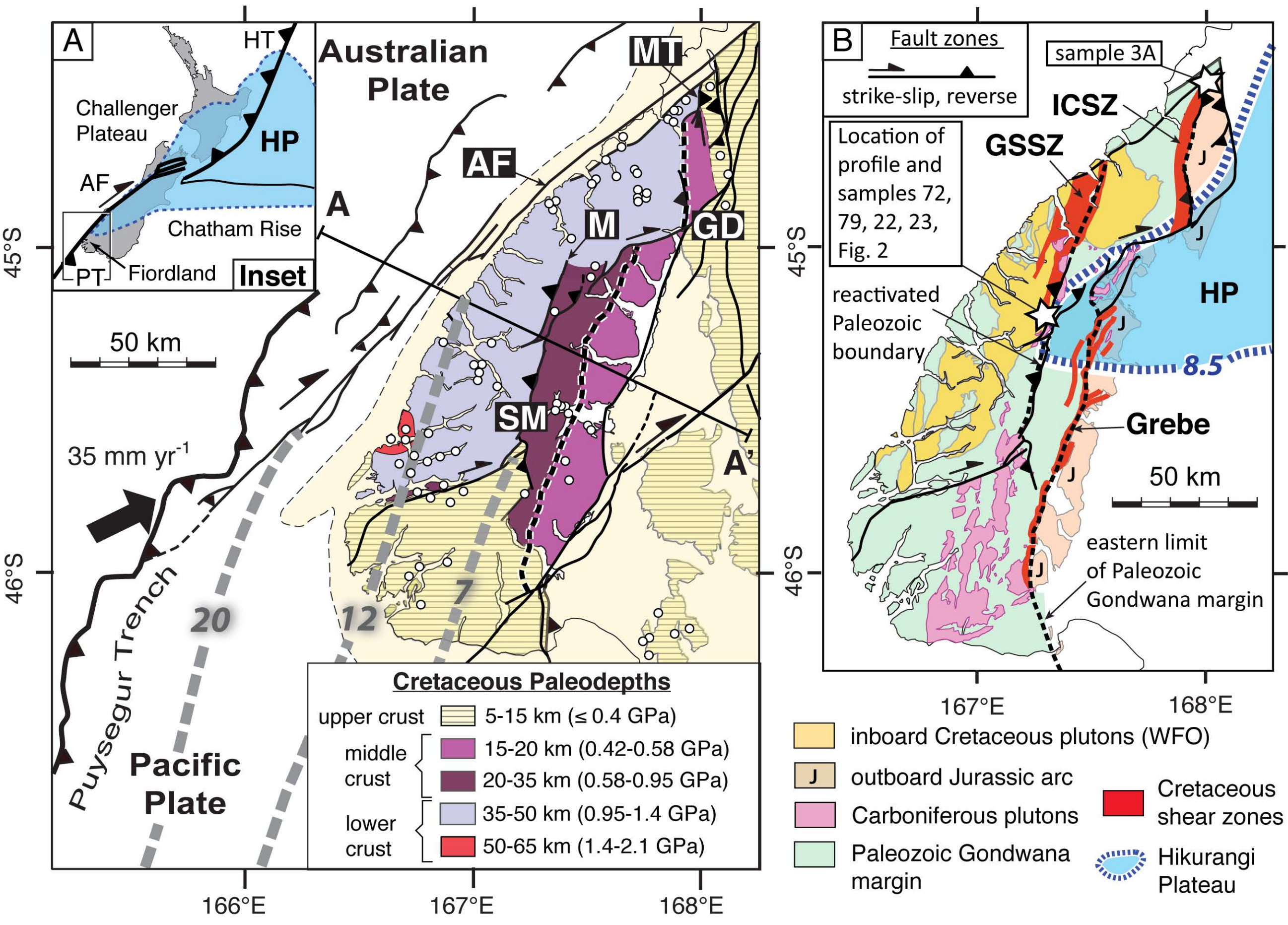
A
Inset
HT
Challenger Plateau
HP
AF
Chatham Rise
PT
Fiordland
Australian Plate
MT
AF
A
M
GD
SM
A'
50 km
35 mm yr-1
Puysegur Trench
Pacific Plate
20
12
7
45°S
46°S
166°E
167°E
168°E
Cretaceous Paleodepths
upper crust
5-15 km (≤ 0.4 GPa)
middle crust
15-20 km (0.42-0.58 GPa)
20-35 km (0.58-0.95 GPa)
lower crust
35-50 km (0.95-1.4 GPa)
50-65 km (1.4-2.1 GPa)
B
Fault zones
strike-slip, reverse
sample 3A
ICSZ
GSSZ
Location of profile and samples 72, 79, 22, 23, Fig. 2
reactivated Paleozoic boundary
HP
J
8.5
Grebe
50 km
eastern limit of Paleozoic Gondwana margin
inboard Cretaceous plutons (WFO)
outboard Jurassic arc
Carboniferous plutons
Paleozoic Gondwana margin
Cretaceous shear zones
Hikurangi Plateau

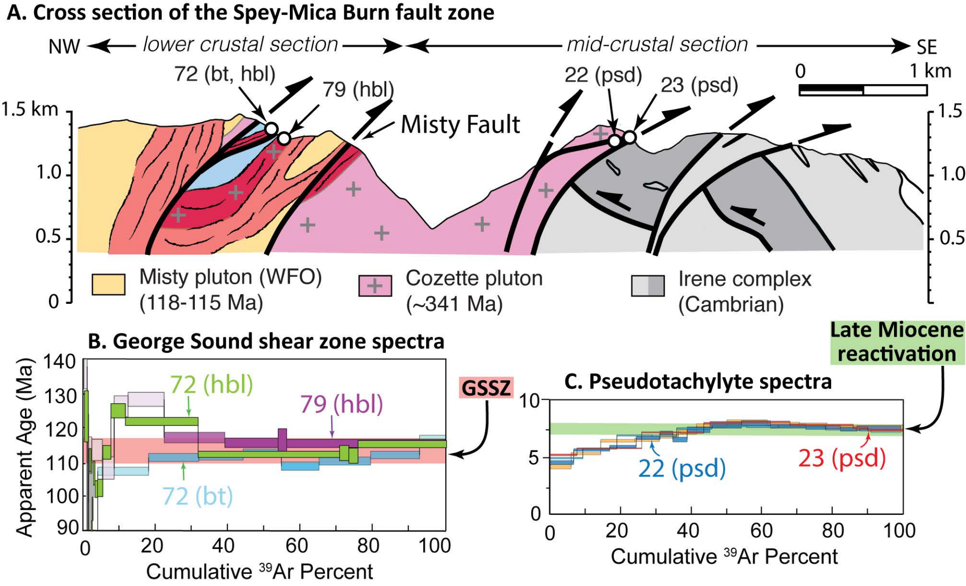

A. Cross section of the Spey-Mica Burn fault zone
NW
lower crustal section
mid-crustal section
SE
72 (bt, hbl)
79 (hbl)
Misty Fault
22 (psd)
23 (psd)
0
1 km
1.5 km
1.0
0.5
0
1.5
1.0
0.5
Misty pluton (WFO)
(118-115 Ma)
Cozette pluton
(~341 Ma)
Irene complex
(Cambrian)
B. George Sound shear zone spectra
Apparent Age (Ma)
140
130
120
110
100
90
72 (hbl)
79 (hbl)
72 (bt)
GSSZ
0
20
40
60
80
100
Cumulative 39Ar Percent
Late Miocene
reactivation
C. Pseudotachylyte spectra
10
5
0
22 (psd)
23 (psd)
0
20
40
60
80
100
Cumulative 39Ar Percent

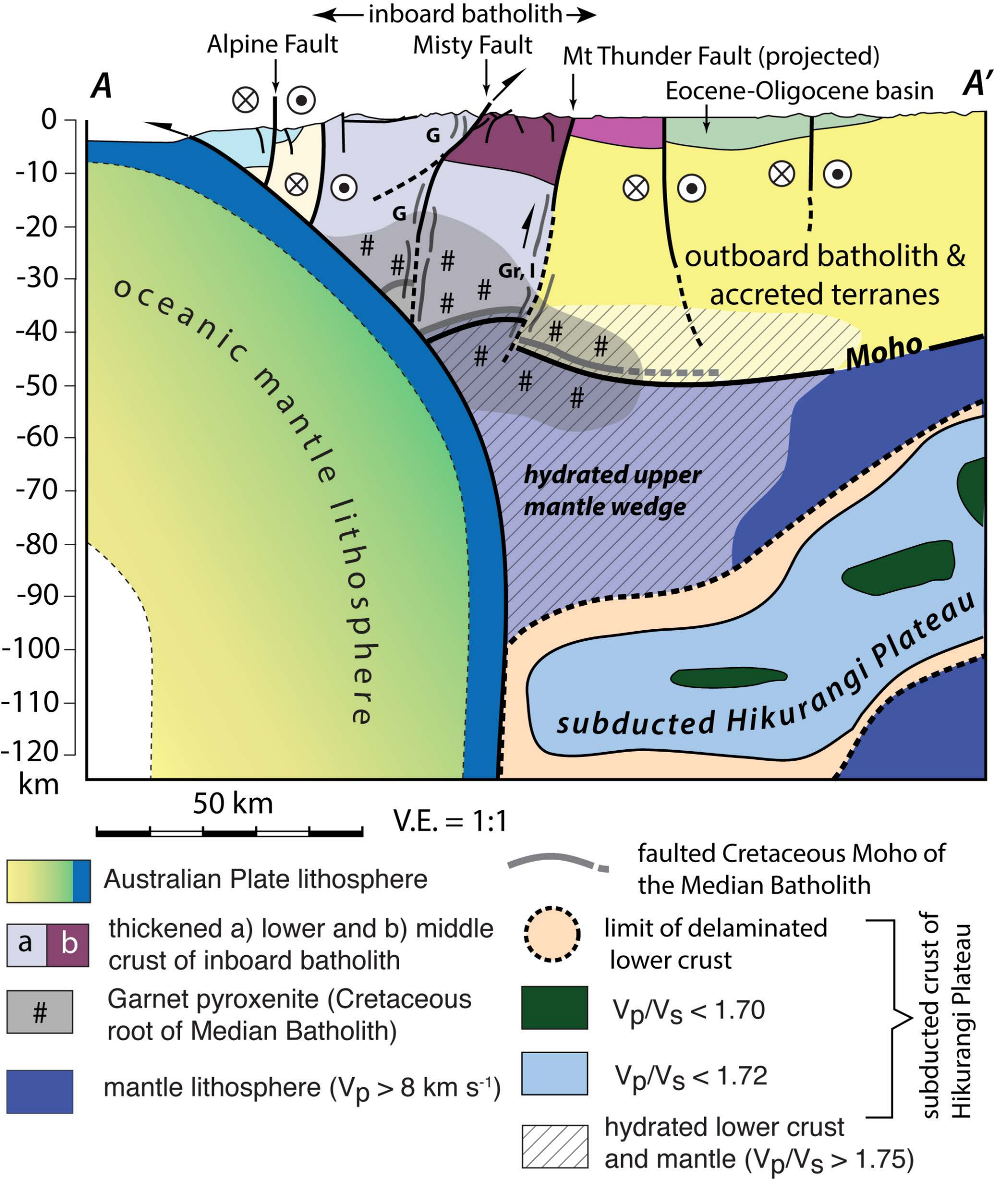

inboard batholith
Alpine Fault
Misty Fault
Mt Thunder Fault (projected)
Eocene-Oligocene basin
A
A′
0
-10
-20
-30
-40
-50
-60
-70
-80
-90
-100
-110
-120
km
G
G
Gr, I
outboard batholith & accreted terranes
Moho
oceanic mantle lithosphere
hydrated upper mantle wedge
subducted Hikurangi Plateau
50 km
V.E. = 1:1
Australian Plate lithosphere
a
b
thickened a) lower and b) middle crust of inboard batholith
#
Garnet pyroxenite (Cretaceous root of Median Batholith)
mantle lithosphere ($V_p > 8$ km s^{-1})
faulted Cretaceous Moho of the Median Batholith
limit of delaminated lower crust
$V_p/V_s < 1.70$
$V_p/V_s < 1.72$
hydrated lower crust and mantle ($V_p/V_s > 1.75$)
subducted crust of Hikurangi Plateau

[1]GSA Data Repository item 201Xxxx, $^{40}Ar/^{39}Ar$ methods and data tables, table of paleodepth data, fault-slip data table, additional references, is available online at www.geosociety.org/pubs/ft20XX.htm, or on request from editing@geosociety.org or Documents Secretary, GSA, P.O. Box 9140, Boulder, CO 80301, USA.

SUPPLEMENTARY DATA

Table 1. Compilation of Cretaceous paleodepth data.

Table 2. Table of representative fault-slip data. Fault plane solutions are plotted in Figure 1 of Supplementary data.

Table 3. Data table summarizing $^{40}Ar/^{39}Ar$ results with sample locations.

Table 4. $^{40}Ar/^{39}Ar$ data tables. Errors are quoted as absolute analytical errors are at the 1σ level unless otherwise noted.

$^{40}Ar/^{39}Ar$ Methods

$^{40}Ar/^{39}Ar$ analyses were performed at the University of Vermont Noble Gas Geochronology Laboratory. Inclusion-free mineral grains, or what appear as clast-free fragments of pseudotachylyte, were handpicked from crushed rock samples under a bioptic microscope after having been washed, sonified, and dried to remove any adhering particulate matter. Grains were loaded into aluminum foil packets, arranged in a suprasil vial, and placed in an aluminum canister for irradiation. Samples were irradiated at the Oregon State University Radiation Center in the CLICIT facility with multigrain aliquots of Fish Canyon Tuff Sanidine to act as a flux monitor. Laser step heating for $^{40}Ar/^{39}Ar$ dating was conducted with a Santa Cruz Laser Microfurnace 75 W diode laser system. Samples were loaded directly into wells in a copper sample holder. The gas released during heating was purified with SAES getters and argon isotopes were analyzed on a Nu Instruments Noblesse magnetic sector noble gas mass spectrometer in peak-hopping mode during step-heating analyses. Data from samples and flux monitors were corrected for blanks, mass discrimination, atmospheric argon, neutron-induced interfering isotopes, and the decay of ^{37}Ar and ^{39}Ar. Mass discrimination was calculated by analyzing known aliquots of atmospheric argon for which the measured ^{40}Ar/^{36}Ar was compared with an assumed atmospheric value of 298.56 (Lee et al., 2006). Correction factors used to account for interfering nuclear reactions for the irradiated samples, J factors, and decay constants are provided with the sample data tables. A linear interpolation was used to calculate J factors for samples based on sample position between flux monitor packets in the irradiation tube. The data analyses were achieved using both an in-house data reduction program and Isoplot 3.0 (Ludwig, 2003). Plateau ages are reported if sufficient criteria were met (see McDougall and Harrison, 1999). Errors on plateaus and weighted mean ages are quoted at the 1σ level and include precision associated with measurement of the irradiation parameter, J, for flux monitors.

Figure 1. Map showing kinematic data from the eastern margin of Fiordland's lower crustal slice. Black dashed lines are two Late Carboniferous crustal boundaries that were reactivated by late Miocene reverse and strike-slip faults. White dots show location of fault-slip data. Selected fault plane solutions are shown on lower hemisphere equal-area stereoplot where black great circles are measured fault planes, gray dots are measured slickenlines, and black arrows show the sense of motion of the hanging wall (shaded red). The maximum (X), intermediate (Y), and minimum (Z) axes of the instantaneous strain ellipsoid are shown for each fault. Note that the reverse faults within the Spey-Mica Burn fault zone (SM) and Misty Fault (M) connect with the Mt. Thunder Fault (MT) and Glade-Darran fault zone (GD) via strike-slip and oblique-slip fault segments.

To illustrate the fault styles in Fig. 1, we plotted kinematic data on lower hemisphere equal-area stereographic projections using the methods of Marrett and Allmendinger (1990), Allmendinger et al. (2012), and references therein. The great circles on each plot show the orientations of fault planes, dots show the orientations of slickenline straia, and arrows show the sense of motion of the hanging wall. Each plot also shows axes of shortening (Z) and extension (X) calculated by bisecting the angle between the pole to the fault plane and the slickenline. The axes always lie at 45° from the lineation within the shear plane (i.e., the plane containing the pole to the fault and the lineation).

Figure 2. Detailed $^{40}Ar/^{36}Ar$ apparent age spectra from all samples discussed in the text. Sample locations are shown in Figures 1B and 2 of the manuscript. (A) Analyses of hornblende (15AB79A) and biotite (15AB72A) yielded plateau ages of 116.1 ± 1.1 and 111.14 ± 0.76 Ma, respectively. Hornblende spectra from sample 15AB72A is similar to sample 15AB79A. (B), (C) Two runs of samples 15AB22D and 15AB23 from the Spey-Mica Burn fault zone each yielded mean plateau ages of 7.659 ± 0.089 Ma and 7.9 ± 1.5 Ma, respectively. Faults that crosscut the pseudotachylyte in both samples resulted in the age gradients seen above with minimum ages of 4–6 Ma. (D) Two runs of sample 05MT3A from the Mt. Thunder Fault yielded a weighted mean age of 6.97 ± 0.18 Ma. See text for further discussion of ages.

Figure 3. Geologic map of the Spey-Mica Burn fault zone showing faulted sections of the Cretaceous George Sound shear zone (map location shown in Figure 1 of main article). Map shows the location of four sample sites shown. M is Misty Fault. Cross section X-X' is shown

in Figure 2A of the accompanying article. Features to north and south of line of section are projected onto the profile.

References

Allibone, A.H., Milan, L.A., Daczko, N.R., and Turnbull, I.M., 2009, Granulite facies thermal aureoles and metastable amphibolite facies assemblages adjacent to the Western Fiordland Orthogneiss in southwest Fiordland, New Zealand: Journal of Metamorphic Geology, v. 27, p. 349–369, doi:10.1111/j.1525-1314.2009.00822.x.

Allmendinger, R.W., Cardozo, N.C., and Fisher, D., 2012, Structural Geology Algorithms—Vectors and tensors: Cambridge, England, Cambridge University Press, 289 p.

Bhattacharya, S., Kemp, A.I.S., and Collins, W.J., 2018, Response of zircon to melting and metamorphism in deep arc crust, Fiordland (New Zealand): implications for zircon inheritance in cordilleran granites:Contributions to Mineralogy and Petrology, v. 173, no. 28, p. 1-36.

Bradshaw, J.Y., 1989, Origin and metamorphic history of an Early Cretaceous polybaric granulite terrain, Fiordland, southwest New Zealand: Contributions to Mineralogy and Petrology, v. 103, p. 346–360, doi:10.1007/BF00402921.

Buritica, L., 2018, Temporal and Spatial Variations in Magmatism and Transpressional Deformation in the Middle to Lower-Crust of a Cretaceous Arc, Median Batholith, Fiordland, New Zealand [M.S. thesis]: California State University Northridge, 124 p.

Clarke, C.L., Klepeis, K.A., and Daczko, N.R., 2000, Cretaceous high-P granulites at Milford Sound, New Zealand: Metamorphic history and emplacement in a convergent margin setting: Journal of Metamorphic Geology, v. 18, p. 359–374, doi:10.1046/j.1525-1314.2000.00259.x.

Clarke, G.L., Fitzherbert, J.A., Milan, L.A., Daczko, N.R. and Degeling, H.S., 2010, Anti-clockwise P-T paths in the lower crust: an example from a kyanite-bearing regional aureole, George Sound, New Zealand: Journal of Metamorphic Geology, v. 28, p. 77–96, doi:10.1111/j.1525-1314.2009.00854.x

Daczko, N., Klepeis, K.A., and Clarke, G.L., 2002, Kyanite-paragonite-bearing assemblages, northern Fiordland, New Zealand: rapid cooling of the lower crustal root to a Cretaceous magmatic arc, *Journal of Metamorphic Geology*, 20, 887-902.

Daczko, N.R., and Halpin, J.A., 2009a, Evidence for melt migration enhancing recrystallization of metastable assemblages in ma c lower crust, Fiordland, New Zealand: Journal of Metamorphic Geology, v. 27, p. 167–185, doi:10.1111/j.1525-1314.2009.00811.x.

Daczko, N.R., Klepeis, K.A., and Clarke, G.L., 2001, Evidence of early Cretaceous collisional-style orogenesis in Northern Fiordland, New Zealand and its effects on the evolution of the lower crust: Journal of Structural Geology, v. 23, p. 693–713, doi: 10.1016/S0191-8141(00)00130-9.

Daczko, N.R., Milan, L.A., and Halpin, J.A., 2009, Metastable persistence of pelitic metamorphic assemblages at the root of a Cretaceous magmatic arc—Fiordland, New Zealand: Journal of Metamorphic Geology, v. 27, p. 233–247, doi: 10.1111/j.1525-1314.2009.00815.x.

Daczko, N.R., Stevenson, J.A., Clarke, G.L., and Klepeis, K.A., 2002b. Successive hydration and dehydration of high-P mafic granofels involving clinopyroxene-kyanite symplectites, Mt. Daniel, Fiordland, New Zealand: Journal of Metamorphic Geology, v. 20, p. 669-682.

Davids, C., 1999, A thermochronological study of southern Fiordland, New Zealand [Ph.D. thesis]: Australian National University, Canberra, 272 p.

De Paoli, M.C., Clarke, G.L., Klepeis, K.A., Allibone, A.H., and Turnbull, I.M., 2009, The eclogite- granulite transition: Mafic and intermediate assemblages at Breaksea sound, New Zealand: Journal of Petrology, v. 50, p. 2307–2343, doi:10.1093/petrology/egp078.

Flowers, R.M., Bowring, S., Tulloch, A.J., and Klepeis, K.A., 2005, Tempo of burial and exhumation within the deep roots of a magmatic arc, Fiordland, New Zealand: Geology, v. 33, p. 17–20, doi:10.1130/G21010.1.

Gollan, M.R., 2006, Plutonic petrogenesis and mineralisation in southwest Fiordland [M.S. thesis]: University of Otago, Dunedin, New Zealand, 220 p.

Hollis, J.A., Clarke, G.L., Klepeis, K.A., Daczko, N.R., and Ireland, T.R., 2003, Geochronology and geochemistry of high-pressure granulites of the Arthur River Complex, Fiordland, New Zealand: Cretaceous magmatism and metamorphism on the palaeo-Pacific Margin: Journal of Metamorphic Geology, v. 21, p. 299–313, doi:10.1046/j.1525-1314.2003.00443.x.

Hollis, J.A., Clarke, G.L., Klepeis, K.A., Daczko, N.R., and Ireland, T.R., 2004, The regional significance of Cretaceous magmatism and metamorphism in Fiordland, New Zealand, from U-Pb zircon geochronology: Journal of Metamorphic Geology, v. 22, p. 607–627, doi:10.1111/j.1525 -1314.2004.00537.x.

Jicha, B.R., and Brown, F.H., 2014, An age for the Korath Range, Ethiopia and the viability of $^{40}Ar/^{39}Ar$ dating of kaersutite in Late Pleistocene volcanics: Quaternary Geochronology, v. 21, p. 53-57.

Kimbrough, D.L., Tulloch, A.J., Coombs, D.S., Landis, C.A., Johnston, M.R., and Mattinson, J.M., 1994, Uranium-lead zircon ages from the Median Tectonic Zone, New Zealand: New Zealand Journal of Geology and Geophysics, v. 37, p. 393–419, doi:10.1080/00288306.1994.9514630.

Kuiper, K.F., Deino, A., Hilgen, F.J., Krijgsman, W., Renne, P.R. and Wijbrans, A.J., 2008, Synchronizing rock clocks of Earth history: Science, v. 320, no. 5875, p. 500-504.

Klepeis, K.A., Daczko, N. R., and Clarke, G.L., 1999, Kinematic vorticity and tectonic significance of superposed mylonites in a major lower crustal shear zone, northern Fiordland, New Zealand: Journal of Structural Geology, v. 21, no. 10, p. 1385-1405.

Klepeis, K.A., Clarke, G.L., Gehrels, G., and Vervoort, J., 2004, Processes controlling vertical coupling and decoupling between the upper and lower crust of orogens: Results from Fiordland, New Zealand: Journal of Structural Geology, v. 26, p. 765–791, doi:10.1016/j.jsg .2003.08.012.

Klepeis, K.A., Schwartz, J.J., Stowell, H.H., and Tulloch, A., 2016, Gneiss domes, vertical and horizontal mass transfer, and the initiation of extension in the hot lower crustal root of a continental arc, Fiordland, New Zealand: Lithosphere, v. 8, p. 116-140, doi:10.1130/L490.1.

Kretz, R., 1983, Symbols for rock-forming minerals: American Mineralogist, v. 68, p. 277 - 279.

Lee, J.Y., Marti, K., Severinghaus, J.P., Kawamura, K., Yoo, H.S., Lee, J.B. and Kim, J.S., 2006, A redetermination of the isotopic abundances of atmospheric Ar: Geochimica et Cosmochimica Acta, v. 70, no. 17, p. 4507-4512.

Marcotte, S.B., Klepeis, K., Clarke, G.L., Gehrels, G., and Hollis, J.A., 2005, Intra-arc transpression in the lower crust and its relationship to magmatism in a Mesozoic magmatic arc: Tectonophysics, v. 407, p. 135–163, doi:10.1016/j.tecto.2005.07.007.

Marrett, R., and Allmendinger, R., 1990, Kinematic analysis of fault-slip data: Journal of Structural Geology, v. 12, p. 973-986.

McDougall, I., Mac Dougall, I., and Harrison, T.M., 1999, Geochronology and Thermochronology by the $^{40}Ar/^{39}Ar$ Method: New York, NY, Oxford University Press, 288 p.

Min, K., Mundil, R., Renne, P.R., and Ludwig, K.R., 2000, A test for systematic errors in 40Ar/39Ar geochronology through comparison with U/Pb analysis of a 1.1-Ga rhyolite:Geochimica et Cosmochimica Acta, v. 64, no. 1, p. 73-98.

Mortimer, N., Gans, P., Calvert, A., and Walker, N., 1999, Geology and thermochronometry of the east edge of the Median Batholith (Median Tectonic Zone): a new perspective on Permian to Cretaceous crustal growth of New Zealand: The Island Arc, v. 8, p. 404–425

Ramezani, J., and Tulloch, A.J., 2009, TIMS U-Pb geochronology of southern and eastern Fiordland: http://data.gns.cri.nz/paperdata/index.jsp, doi: 10.21420/G2CC7Z.

Renne, P.R., Deino, A.L., Hilgen, F.J., Kuiper, K.F., Mark, D.F., Mitchell, W.S., Morgan, L.E., Mundil, R., and Smit, J., 2013, Time scales of critical events around the Cretaceous-Paleogene boundary: Science, v. 339, no. 6120, p. 684-687.

Renne, P.R., Swisher, C.C., Deino, A.L., Karner, D.B., Owens, T.L., and DePaolo, D.J., 1998, Intercalibration of standards, absolute ages and uncertainties in $^{40}Ar/^{39}Ar$ dating: Chemical Geology, v. 145, no. 1-2, p. 117-152.

Schwartz, J.J., Stowell, H.H., Klepeis, K.A., Tulloch, A.J., Kylander-Clark, A.R.C., Hacker, B.R., and Coble, M.A., 2016, Thermochronology of extensional orogenic collapse in the deep crust of Zealandia: Geosphere, v. 12, p. 647–677, doi:10.1130/GES01232.1.

Scott, J. M., and A. F. Cooper, 2006, Early Cretaceous extensional exhumation of the lower crust of a magmatic arc: Evidence from the Mount Irene Shear Zone, Fiordland, New Zealand: Tectonics, v. 25, TC3018, doi:10.1029/2005TC001890.

Scott, J. M., and Palin, J.M., 2008, LA-ICP-MS U-Pb zircon dates from Mesozoic plutonic rocks in eastern Fiordland, New Zealand: New Zealand Journal of Geology and Geophysics, v. 51, p. 105-113.

Scott, J. M., Palin, J.M., and Cooper, A.F., 2009a, A younger age constraint on high-grade metamorphism near George Sound in Fiordland, New Zealand: New Zealand Journal of Geology and Geophysics, v. 52, p. 67-71.

Scott, J.M., Cooper, A.F., Palin, J.M., Tulloch, A.J., Kula, J., Jongens, R., Spell, T.L., and Pearson, N., 2009c, Tracking the influence of continental margin on growth of a magmatic arc in Fiordland, New Zealand using thermobarometry, thermochronology and zircon U–Pb and Hf isotopes: Tectonics. TC6007 doi:10.1029/2009TC002489.

Scott, J.M., Cooper, A.F., Tulloch, A.J., and Spell, T.L., 2011, Crustal thickening of the Early Cretaceous paleo-Pacific Gondwana margin: Gondwana Research, v. 20, p. 380-394.

Scott, J.M., Palin, J.M., Cooper, A.F., Fagereng, Å., and King, R.P., 2009b, Polymetamorphism, zircon growth and retention of early assemblages through evolution of the Fiordland continental margin: Journal of Metamorphic Geology, v. 27, p. 281–294.

Steiger, R., and Jäger, E., 1977, Subcommission on geochronology: convention on the use of decay constants in geo-and cosmochronology: Earth and Planetary Science Letters, v. 36, no. 3, p. 359-362.

Stowell, H., Odom Parker, K., Gatewood, M., Tulloch, A., and Koenig, A., 2014, Temporal links between pluton emplacement, garnet granulite metamorphism, partial melting and extensional collapse in the lower crust of a Cretaceous magmatic arc, Fiordland, New Zealand: Journal of Metamorphic Geology, v. 32, p. 151-175, doi:10.1111/jmg.12064

Stowell, H.H., Tulloch, A., Zuluaga, C.A., and Koenig, A., 2010, Timing and duration of garnet granulite metamorphism in magmatic arc crust, Fiordland, New Zealand: Chemical Geology, v. 273, p. 91–110, doi:10.1016/j .chemgeo.2010.02.015.

Stowell, Harold H., Schwartz, J.J., Klepeis, K.A., Hout, C., Tulloch, A.J., and Koenig, A., 2017, Sm-Nd garnet ages for granulite and eclogite in the Breaksea Orthogneiss and widespread granulite facies metamorphism of the lower crust, Fiordland magmatic arc, New Zealand: Lithosphere, v. 9, no. 6, p. 953-975, https://doi.org/10.1130/L662.1

Tulloch, A.J., and Challis, G.A., 2000, Emplacement depths of Paleozoic-Mesozoic plutons from western New Zealand estimated by hornblende-Al geobarometry: New Zealand Journal of Geology and Geophysics, v. 43, p. 555-567.

Tulloch, A.J., Ireland, T.R., Kimbrough, D.L., Griffin, W.L., and Ramezani, J., 2010, Autochthonous inheritance of zircon through Cretaceous partial melting of Carboniferous plutons: The Arthur River Complex, Fiordland, New Zealand: Contributions to Mineralogy and Petrology, v. 161, p. 401–421, doi: 10.1007/s00410-010-0539-6.

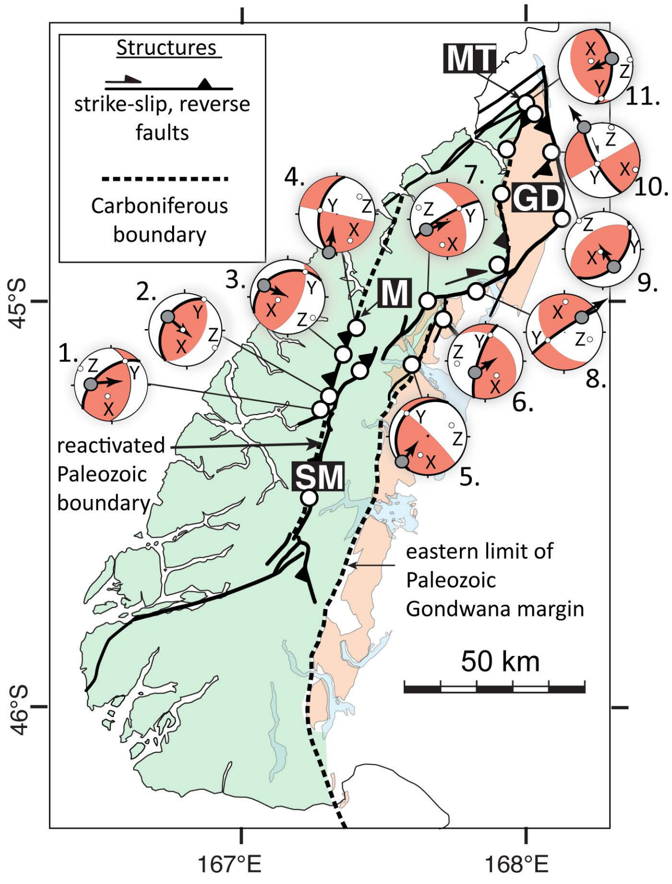

Structures
strike-slip, reverse faults
Carboniferous boundary
MT
GD
M
SM
reactivated Paleozoic boundary
eastern limit of Paleozoic Gondwana margin
50 km
45°S
46°S
167°E
168°E
1.
2.
3.
4.
5.
6.
7.
8.
9.
10.
11.

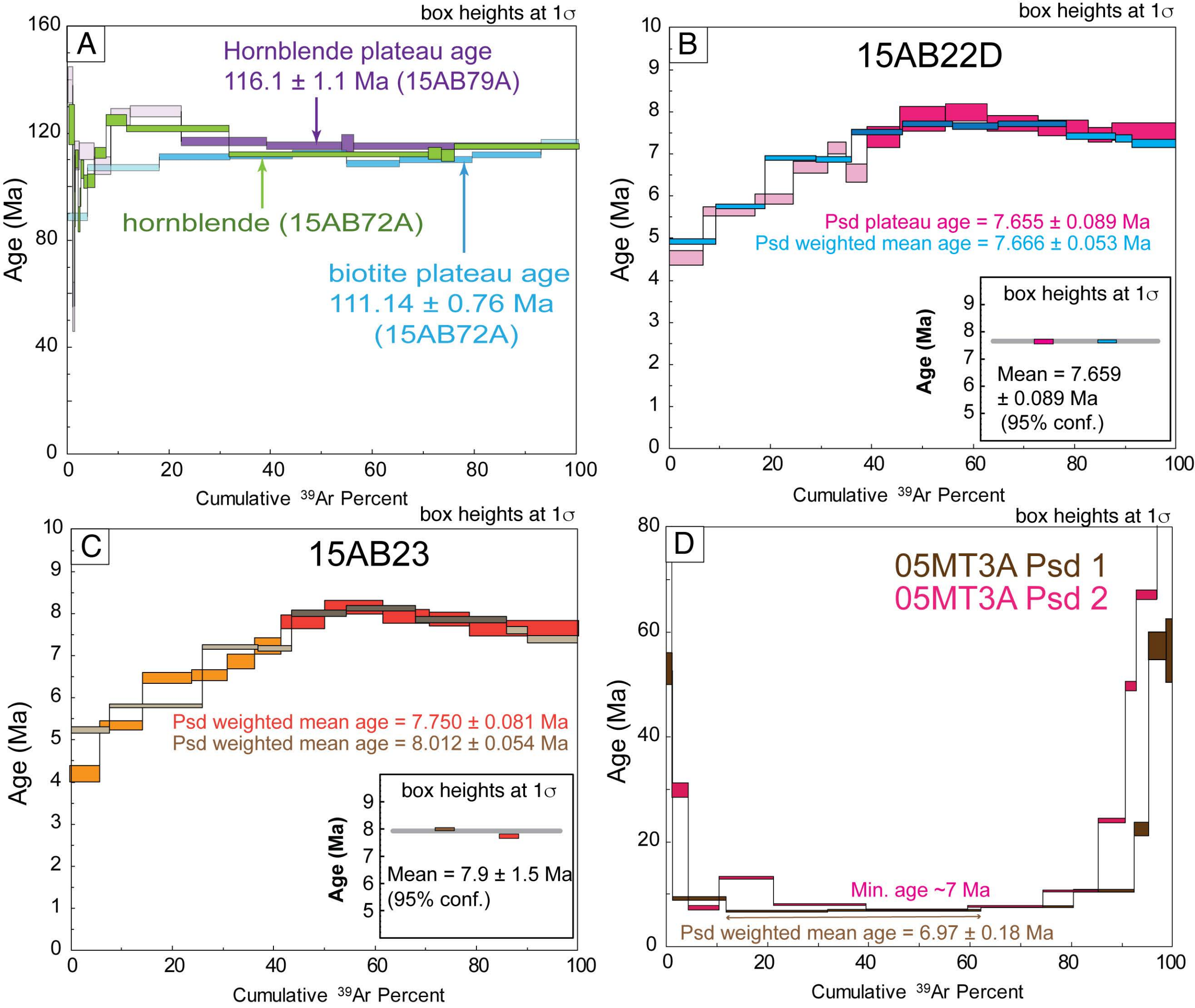
A
box heights at 1σ
Hornblende plateau age
116.1 ± 1.1 Ma (15AB79A)
hornblende (15AB72A)
biotite plateau age
111.14 ± 0.76 Ma
(15AB72A)
Age (Ma)
Cumulative 39Ar Percent
B
15AB22D
box heights at 1σ
Psd plateau age = 7.655 ± 0.089 Ma
Psd weighted mean age = 7.666 ± 0.053 Ma
Mean = 7.659
± 0.089 Ma
(95% conf.)
Age (Ma)
Cumulative 39Ar Percent
C
15AB23
box heights at 1σ
Psd weighted mean age = 7.750 ± 0.081 Ma
Psd weighted mean age = 8.012 ± 0.054 Ma
Mean = 7.9 ± 1.5 Ma
(95% conf.)
Age (Ma)
Cumulative 39Ar Percent
D
box heights at 1σ
05MT3A Psd 1
05MT3A Psd 2
Min. age ~7 Ma
Psd weighted mean age = 6.97 ± 0.18 Ma
Age (Ma)
Cumulative 39Ar Percent

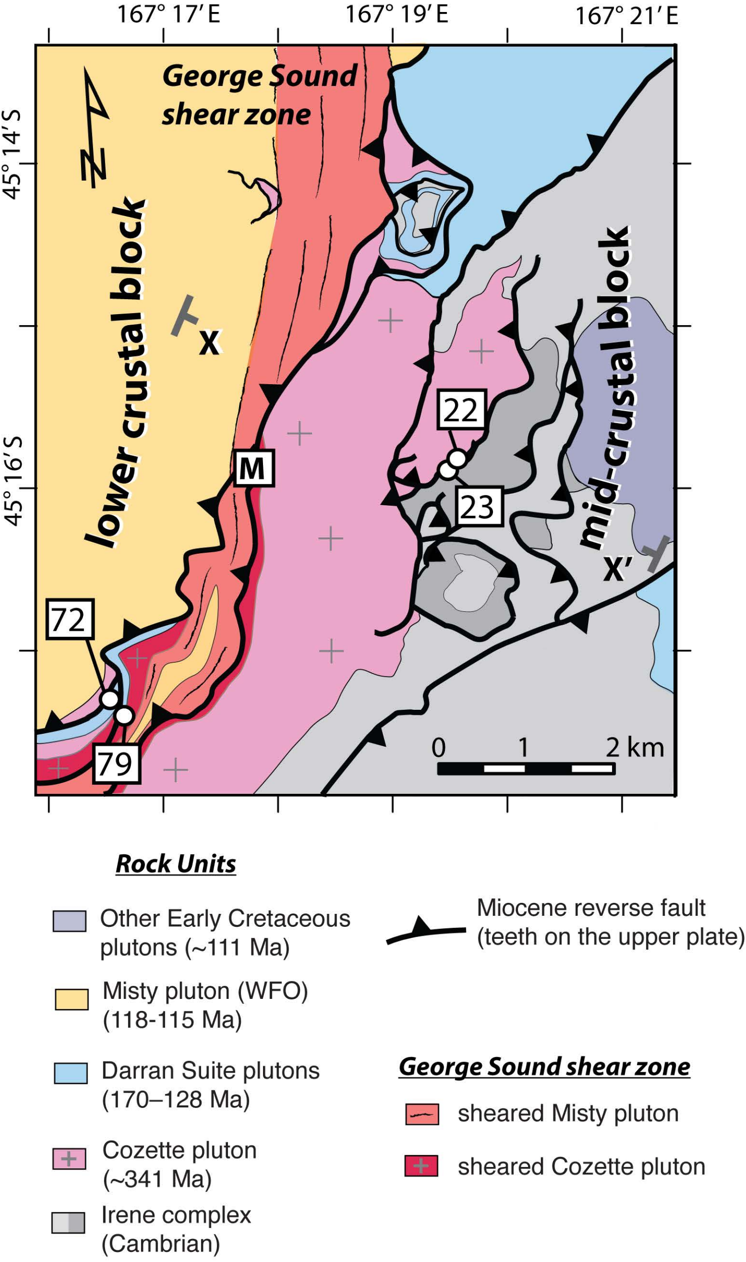

167° 17′ E
167° 19′ E
167° 21′ E
45° 14′ S
45° 16′ S
George Sound shear zone
N
lower crustal block
mid-crustal block
X
X′
M
22
23
72
79
0
1
2 km
Rock Units
Other Early Cretaceous plutons (~111 Ma)
Misty pluton (WFO) (118-115 Ma)
Darran Suite plutons (170–128 Ma)
Cozette pluton (~341 Ma)
Irene complex (Cambrian)
Miocene reverse fault (teeth on the upper plate)
George Sound shear zone
sheared Misty pluton
sheared Cozette pluton

Table 1. Summary of published paleodepth data and metamorphic ages.

Division (Cretaceous)	Location	Map Unit	Rock Type	Minerals	Pressure Range* (kbar)	References (barometry)	Metamorphic Ages[#] (Ma)	References (ages)
LOWER CRUST								
	Stirling Valley	Pembroke Granulite	garnet granulite	Grt-Cpx-Pl-Qtz-Ky	16.1-13.7	1	n.d.	
	Pembroke Valley	Pembroke granulite	garnet granulite	Grt-Cpx-Pl-Qtz	16.6, 14.7	1	126.1 ± 2.0[c] to 122.6 ± 2.0[c]	2
	Pembroke Valley	Pembroke granulite	garnet granulite	Grt-Cpx-Hbl-Pl-Qtz	14-11	2	126.1 ± 2.0[c] to 122.6 ± 2.0[c]	2
	Pembroke Valley	Pembroke granulite	garnet amphibolite	Grt-Hbl-Czo-Bt-Pl-Rt	14.1 ± 1.2	3	119-111[b], 118-110[e]	9, 29
	Pembroke Valley	Pembroke granulite	garnet amphibolite	Ky-Pg-Phg	13-11	5	119-111[b], 118-110[e]	9, 29
	Lake Pukutahi	Miford orthogneiss	garnet amphibolite	Grt-Hbl-Phg-Pl-Czo-Qtz	10.9-13.5	5	115.7 ± 3.8[b], 115.0 ± 3.6[b]	8, 9
	Lake Pukutahi	Miford orthogneiss	garnet amphibolite	Grt-Hbl-Phg-Pl-Czo-Qtz	13-11	5	119-111[b], 118-110[e]	9, 29
	Mt. Daniel	Miford orthogneiss	garnet amphibolite	Grt-Cpx-Hbl-Pl-Qtz	15-14	5	119-111[b], 117.4 ± 3.1 to ~114[b], 118-110[e]	9, 20, 29
	Mt. Daniel	Worsley pluton	garnet granulite	Grt-Cpx-Pl-Qtz-Ky-Hbl	14-13	4	121.8 ± 1.7[d], 117.4 ± 3.1 to ~114[b]	6, 20
	Mt Daniel	Miford orthogneiss	mafic granulite	Cpx-Pl-Qtz	12.4	11	~120[d],[f], 117.4 ± 3.1 to ~114[b]	22, 21, 20
	Poison Bay	Worsley pluton	garnet granulite	Grt-Cpx-Pl-Qtz	12.6 ± 1.9	1	n.d.	
	Poison Bay	Thurso Gneiss	Metapelitic gneiss	Grt-Hbl-Pl-Bt-Rt-Czo	11.9 ± 1.1	7	n.d.	
	Poison Bay	Worsely pluton	garnet granulite	Grt-Cpx-Bt-Pl ± Opx	15-11	11	n.d.	
	Hunter Pass	Undiff. Paragneiss	metapelite	Grt-Pl-Ky-Qtz	12.2-11.7	11	119.1-120.1[g]	23
	Sutherland Sound	Worsely pluton	garnet granulite	Grt-Cpx-Pl-Qtz	13-11	11	n.d.	
	Bligh Sound	Worsely pluton	garnet granulite	Grt-Cpx-Pl-Qtz	13.3-11	11	n.d	
	George Sound	G. Sound paragneiss	paragneiss	Pl-Grt-Ky-Qtz	12.2-11.7	11	117.2 ± 1.3[d]	6
	George Sound	G. Sound paragneiss	migmatite	Grt-Hbl-Bt-Ep-Pl-Qtz	12-11	6	117.2 ± 1.3[d]	6
	George Sound	G. Sound paragneiss	migmatite	Ky-Bt-Grt-Pl-Ms-Pg	11	12	117.2 ± 1.3[d]	6
	Caswell Sound	G. Sound paragneiss	paragneiss	Grt-Bt-Pl-Kfs	n.d.		113.6 ± 2.3[e]	18
	Lake Grave	Worsely pluton	garnet granulite	Grt-Cpx-Pl-Qtz-Pg	14.5-12	10	115.3 ± 0.7[b]	10
	Mt Daniel	Worsely pluton	diorite	Cpx-Opx- Hbl ± Czo	11-6	6	121.H178 ± 1.7d	6
	Bradshaw Sound	Misty pluton	garnet granulite	Grt-Cpx-Bt-Pl-Qtz	12-10.5	16	109.2 ± 2.0[c], 114.5 ± 2.3[e]	16, 18
	Doubtful Sound	Malaspina pluton	garnet granulite	Grt-Cpx-Pl-Rt ± Qtz	15-14	15	115.6 ± 2.6 to 110.6 ± 2.0[c]	15
	Doubtful Sound	Deep Cove Gneiss	garnet paragneiss	Grt-Bt-Ms-Czo-Ky-Pl-Qtz-Rt-Ttn	10	6	117.2 ± 0.8[a], , 113.5 ± 1.7[a], 116.3 ± 1.7[a]	19, 18
	Crooked Arm	Malaspina pluton	garnet granulite	Grt-Cpx-Pl-Rt ± Qtz	15-14	15	114.0 ± 2.2[d], 112.5 ± 1.1[c]	6, 15
	Breaksea Entrance	Breaksea orthogneiss	garnet granulite	Grt-Omp-Pl-Kfs-Rt-Ky-Qtz-Ap	21-18	13	111-108[c], 115-111[a]	14
	Breaksea Entrance	Breaksea orthogneiss	eclogite	Grt-Omp-Opx	21-19	13	123-120[a, c]	14
	Acheron Passage	Malaspina pluton	garnet granulite	Rt	15-12	13	111.9 ± 1.6[c], 118.0 ± 1.8[b]	15
	Breaksea Entrance	Breaksea orthogneiss	eclogite	Grt-Bt-Ilm-Hbl-Cpx-Rt-Scp	18-15.5	14	123-120[a, c]	14
	Breaksea Sound	Malaspina pluton	garnet granulite	Grt-Cpx-Pl-Qtz-Rt	13.5-10.2	17	113.5 ± 1.7[a], 111.4 ± 2.2[e]	19, 18
	Resolution Island	Deep Cove Gneiss	calcareous gneiss	Grt-Cpx-Ky-Wo-Qtz-Ttn-Scp	14-10	17	113.9 ± 1.6[a], 110.4 ± 2.2[e], 114-109[h]	18, 24
	Wet Jacket Sound	Deep Cove Gneiss	metapsammite	Grt-Hbl-Bt-Pl-Qtz-Rt-Ttn	14-10	17	115.3 ± 2.3[e]	18
	Resolution Island	Malaspina pluton	migmatitic granulite	Grt-Cpx-Opx-Hbl-Pl-Bt-Rt	14-12.5	15	111.9 ± 1.6[c]	15
MIDDLE CRUST	Marguerite Peaks	Marguerite Amphibolite	amphibolite	Mrg-Ky-St-Chl-Pl	8.8 ± 0.6	25	119-117[b]	25, 26
	West of Grebe	Puteketeke pluton	granodiorite, tonalite	Hbl-Bt-Pl-Kfs-Qtz-Ttn	7.1-5.5	27	120.9 ± 0.9[b], 121.8 ± 1.7[a], 118-115[c], 111. ± 1.6[i]	28, 29, 30
	West of Grebe	Refrigerator orthogneiss	tonalite	Qtz-Hbl-Pl	7.2-6.1	27	120.7 ± 1.7[b], 123-118[c], 112.7 ± 1.3[i]	28, 29, 30
	East of Dusky Sound	Russet Formation	paragneiss	Grt-Bt-Pl	7.5 ± 1.2	27	n.d.	
	Grebe shear zone	Grebe Mylonite	mylonitic orthogneiss	Grt-Bt-Hbl-Pl-Qtz	7.5 ± 1.2	27, 30	125-116[c], 115-110[i]	29, 30
	East of Grebe	Takahe Pluton	granodiorite	Hbl-Bt-Pl-Kfs-Qtz-Ttn	7.5-5.3	27	125-123[c]	29
	East of Grebe	Hunter Intrusives	paragneiss	Grt-Bt-Pl	4.2 ± 1.2	27	116.3 ± 1.7[c], 122-117[i]	29, 30
	East of Grebe	Mt Crescent Formation	paragneiss	Grt-Bt-Pl	5.2 ± 1.2	27	<124[b]	27
	Mt Irene	Robin Gneiss	garnet amphibolite	Grt-Hbl-Pl-Qtz	8.5 ± 2.2	32	125-116[c], 115-110[i]	29, 30
	Lake Manapouri	Manapouri granodiorite	granodiorite	Hbl-Bt-Pl-Kfs-Qtz-Ttn	5.8-5.5	32	151.9 ± 1[j]	33
	Dusky Sound	Deep Cove Gneiss	migmatitic metapelite	Grt-Pl-Bt-Ky-Ms-Qtz-Ilm	7.5	24	107 ± 2 to 105 ± 4[h]	24
	Dusky Sound	Anchor Island Intruisves #2	granite	Bt-Ms-Kfs-Qtz	n.d.		115 ± 1.7[f]	34
UPPER CRUST	Darran Range	Mistake diorite	granodiorite	Hbl-Bt-Pl-Kfs-Qtz-Ttn	3.3-2.1	32, 35	224.2 ± 1[j], 211.8 ± 2.4[i]	33, 35

Skippers Range	Slip Hill granodiorite	granodiorite	Hbl-Bt-Pl-Kfs-Qtz-Ttn	4.4-2.7	32	228.6 ± 1[j]	33
Longwood Range	Holly Burn Intrusives	granodiorite	Hbl-Bt-Pl-Ep-Qtz-Ttn	3.3-1.9	35	228-219[i]	35
Longwood Range	Pourakino Trondhjemite	leucotonalite	Hbl-Bt-Pl-Ep-Qtz-Ttn	2.9-1.8	35	251.2 ± 0.4[i]	35
MacKay Creek	Rotoiti Gneiss	garnet-biotite gneiss	Hbl-Bt-Grt	2-3	35	218-216[i]	35
Hut Creek	Rotoiti Gneiss	garnet-biotite gneiss	Hbl-Bt-Grt	2-3	35	222.1 ± 5.0[i]	35
SW Fiordland	Preservation intrusive Complex	diorite, granite	Pl-Qtz-Kfs-Phg-Hbl ± Grt	2.7-0.8	36	132-122[b]	36
N. of Dusky Sound	Supper Cove Orthogneiss	hornblende-biotite gneiss	Ky-Sil-Hbl-Bt-Ep-Pl-Qtz	8-6	37	100-90[i]	37
S. of Dusky Sound	Paleozoic metasediments	schist and gneiss	And-Sil-Ky-Grt	3-4	37	120-98[i]	37

Notes

* Ranges derive from multiple samples and methods and include errors (±1 kbar unless otherwise noted).

[#] For methods and grid locations see referenced sources.

1 kbar = 3.7 km after Allibone et al. (2009b).

Mineral Abbreviations from Kretz (1983).

Method of age determination

[a]SHRIMP-RG (sensitive high-resolution ion microprobe–reverse geometry) ^{206}U/^{238}Pb metamorphic zircon ages

[b] LA-ICP-MS (laser-ablation-inductively coupled mass spectrometry) ^{206}Pb/^{238}U metamorphic zircon ages

[c]Sm-Nd garnet isochrons

[d]SHRIMP I (sensitive high-resolution ion microprobe) and SHRIMP RG ^{206}U/^{238}Pb metamorphic zircon ages

[e]LASS, ICP-MS (laser ablation split stream inductively coupled plasma– mass spectrometry) metamorphic titanite ages (lower intercepts calculated from regression of ^{207}Pb/^{206}Pb-^{238}U/^{206}Pb data)

fIsotope Dilution Thermal Ionisation Mass Spectrometry (ID-TIMS) and SHRIMP-RG U–Pb analyses of zircons

[g]Analyses of ^{206}Pb/^{238}U on titanite using a VG Sector 54 mass spectrometer

[h] U–Th–Pb analyses of monazite using a Cameca SX100 electron microprobe

[i] ^{40}Ar/^{39}Ar incremental step-heating analyses of biotite, white mica, and/or hornblende

[j]Isotope dilution thermal ionisation mass spectrometry ^{206}Pb/^{238}U dates on zircon.

Sources

1 Clarke et al. (2000)
2 Stowell et al. (2010)
3 Daczko et al. (2001)
4 Daczko et al. (2002b)
5 Daczko et al. (2002a)
6 Hollis et al. (2004)
7 Klepeis et al. (1999)
8 Klepeis et al. (2004)
9 Marcotte et al. (2005)
10 Daczko & Halpin (2009)
11 Bradshaw (1989)
12 Clarke et al. (2010)
13 De Paoli et al. (2009)
14 Stowell et al. (2017)
15 Stowell et al. (2014)
16 H. Stowell, personal communication (2013)
17 Allibone et al. (2009)
18 Schwartz et al. (2016)
19 Klepeis et al. (2016)
20 Bhattacharya et al. (2018)
21 Tulloch et al. (2010)
22 Hollis et al. (2003)
23 Flowers et al. (2005)
24 Daczko et al. (2009)
25 Scott et al. (2009a)
26 Scott et al. (2009b)
27 Scott et al. (2009c)

28	Scott and Palin (2008)
29	Buritica (2018)
30	Scott et a. (2011)
31	Tulloch and Challis (2000)
32	Scott and Cooper (2006)
33	Kimbrough et al. (1994)
34	Ramezani & Tulloch (2009)
35	Mortimer et al. (1999)
36	Gollan (2006)
37	Davids (1999)

Table 2. Representative fault-slip data (fault plane solutions plotted in Fig. 1 of Supplementary Materials).

Plot number (Fig. 1)	**Site Name**	**Location**		**Fault zone**	**Fault-slip data**		
		Northing	**Easting**		**Fault Surface**	**Lineation**	**Sense**
1	15AB90	4970536.2	1151081.5	Spey-Mica Burn fault zone	230 56 NW	272 45	reverse
2	15AB17	4974174.3	1154855.9	Spey-Mica Burn fault zone	202 18 NW	310 17	reverse
3	19MT09	4987733	1156368	Spey-Mica Burn fault zone	244 34 NW	295 28	reverse
4	19MT36	4995952	1159224	Spey-Mica Burn fault zone	192 52 W	192 00	dextral
5	S of Middle fjord	4981300	1170700	unnamed, Murchison Mts.	210 22 W	225 05	dextral-reverse
6	18NF170	5000196	1183272	North Fjord fault	198 75 W	222 57	dextral-reverse
7	19LR53	5003315	1177124	Howitt Peaks Fault	240 80 NW	247 34	dextral-reverse
8	18WA158	5008904.2	1194233.9	Sandfly fault	056 84 NW	40 NE	dextral strike-slip
9	MC06	5046512.5	1209762.5	central Glade-Darran fault	042 45 S	148 41	reverse
10	MC06	5046512.5	1209762.5	central Glade-Darran fault	330 76 W	160 02	dextral strike-slip
11	SMT06	5056935.0	1203695.0	Mt Thunder fault	000 54 E	063 52	reverse

Location coordinates reported in New Zealand Transverse Mercator 2000 (NZTM) projection, horizontal datum NZGD2000.

Table 3. Data table summarizing $^{40}Ar/^{39}Ar$ results with sample locations.

Sample	Fault Zone	Mineral/Rock type	Location Northing	Location Easting	Phase (Aliquot)	PA (Ma)	WMA (Ma)	1σ Error (Ma)	%^{39}Ar	MSWD	Minimum age (Ma)	TFA (Ma)	1σ Error (Ma)
72	Spey-Mica Burn fault zone	Biotite	4971333.07	1150951.41	bt1	111.14		0.76	74.8	1.4	89	110.1	0.4
72	Spey-Mica Burn fault zone	Hornblende	4971333.07	1150951.41	hbl1						88	115.4	0.5
79	Spey-Mica Burn fault zone	Hornblende	4971063.44	1150771.15	hbl1	116.1		1.1	77.7	0.23	56	118.6	0.7
22	Spey-Mica Burn fault zone	pseudotachylyte	4974297.58	1155100.4	psd1	7.666	7.666	0.053	42.3	1.8	4.9	7.04	0.02
22	Spey-Mica Burn fault zone	pseudotachylyte	4974297.58	1155100.4	psd2	7.655		0.089	60.9	0.95	4.6	7.00	0.06
23	Spey-Mica Burn fault zone	pseudotachylyte	4974311.62	1155125.44	psd1		8.012	0.054	42.4	3.8	5.3	7.18	0.02
23	Spey-Mica Burn fault zone	pseudotachylyte	4974311.62	1155125.44	psd2		7.750	0.081	58.5	1.13	4.1	6.97	0.06
3A	Mt Thunder fault zone	pseudotachylyte	5059051.3	1204315.0	psd1		6.97	0.18	50.3	0.55	6.9	11.1	0.2
3A	Mt Thunder fault zone	pseudotachylyte	5059051.3	1204315.0	psd2						7.1	17.8	0.2

Notes:

Location coordinates reported in New Zealand Transverse Mercator 2000 (NZTM) projection, horizontal datum NZGD2000.

PA = plateau age, if more than 3 consecutive steps comprising > 60% of the gas released are concordant

WMA = weighted mean age, calculated in the case where consecutive steps give similar ages but do not define a plateau

MSWD = mean square weighted deviation

TFA=Total Fusion age

Table 4. ^{40}Ar/^{39}Ar Data Tables.

All errors quoted as absolute errors at the 1σ level unless noted as a percentage.

The sample data below were from two separate irradiation batches. Data relevant to calculations (e.g. decay constants and correction factors) are listed at the end based on batch number.

Sample #	Phase	J factor	J abs err	Batch Number															
72	Bt	1.09379E-03	5.78627E-06	UVM005															
Watts	**Time (min)**	**^{38}Ar/^{39}Ar**	**^{38}Ar/^{39}Ar error**	**^{37}Ar/^{39}Ar**	**^{37}Ar/^{39}Ar error**	**^{36}Ar/^{39}Ar**	**^{36}Ar/^{39}Ar error**	**^{39}Ar (cps)**	**^{39}Ar error**	**Cumul % ^{39}Ar**	**% ^{40}Ar***	**^{40}Ar*/^{39}Ar**	**Age (yrs)**	**Age error (yrs)**	**% error**	**^{39}Ar/^{40}Ar**	**^{39}Ar/^{40}Ar error**	**^{36}Ar/^{40}Ar**	**^{36}Ar/^{40}Ar error**
3.8	1	1.62206E-02	7.80637E-04	-3.51020E-01	-2.96350E-01	2.47645E-02	1.31667E-03	903.5	12.1	3.91	86.2	4.61981E+01	8.89330E+07	1.45159E+06	1.6322282	1.86758E-02	2.55307E-04	4.62497E-04	2.38319E-05
3.9	1	1.69163E-02	5.50848E-04	3.11050E-01	8.95309E-02	2.11994E-02	7.82329E-04	3232.0	29.9	17.88	89.8	5.60078E+01	1.07266E+08	1.21582E+06	1.1334685	1.60775E-02	1.50370E-04	3.40834E-04	1.21874E-05
4	1	1.62493E-02	5.18910E-04	2.27983E-01	8.94391E-02	1.68854E-02	6.80233E-04	3235.2	29.9	31.86	92.0	5.81895E+01	1.11318E+08	1.23129E+06	1.1061091	1.58478E-02	1.47386E-04	2.67597E-04	1.04971E-05
4.1	1	1.58000E-02	6.24536E-04	1.34985E-01	9.95082E-02	1.48783E-02	4.68024E-04	2798.6	28.1	43.96	92.9	5.84201E+01	1.11745E+08	1.31300E+06	1.1749939	1.59379E-02	1.61474E-04	2.37129E-04	7.07698E-06
4.25	1	1.70121E-02	6.65409E-04	3.96455E-01	1.17535E-01	1.42983E-02	5.26832E-04	2464.2	23.6	54.61	93.2	5.88687E+01	1.12577E+08	1.26897E+06	1.1272024	1.58764E-02	1.53321E-04	2.27005E-04	8.08264E-06
4.45	1	1.40542E-02	3.65457E-04	-3.34333E-01	-1.36542E-01	1.34962E-02	5.21833E-04	2389.4	24.5	64.94	93.4	5.68115E+01	1.08759E+08	1.30276E+06	1.197839	1.64523E-02	1.71219E-04	2.22044E-04	8.28629E-06
4.7	1	1.58435E-02	6.20067E-04	2.72533E-02	9.82315E-02	1.38620E-02	4.09240E-04	3320.6	32.3	79.30	93.3	5.76219E+01	1.10264E+08	1.25910E+06	1.1418922	1.62189E-02	1.59101E-04	2.24827E-04	6.27439E-06
5	1	1.52241E-02	5.34214E-04	2.32314E-02	1.08373E-01	1.37353E-02	4.28943E-04	3100.1	29.1	92.70	93.4	5.85609E+01	1.12006E+08	1.24196E+06	1.1088251	1.59856E-02	1.51446E-04	2.19567E-04	6.54608E-06
fuse	1	1.64613E-02	7.78470E-04	-4.25558E-01	-1.99134E-01	1.44623E-02	6.87101E-04	1688.5	18.8	100.00	93.4	6.09145E+01	1.16366E+08	1.48206E+06	1.2736203	1.53427E-02	1.72390E-04	2.21892E-04	1.02546E-05

Sample #	Phase	J factor	J abs err	Batch Number															
72	Hbl	1.09497E-03	6.25957E-06	UVM005															
Watts	**Time (min)**	**^{38}Ar/^{39}Ar**	**^{38}Ar/^{39}Ar error**	**^{37}Ar/^{39}Ar**	**^{37}Ar/^{39}Ar error**	**^{36}Ar/^{39}Ar**	**^{36}Ar/^{39}Ar error**	**^{39}Ar (cps)**	**^{39}Ar error**	**Cumul % ^{39}Ar**	**% ^{40}Ar***	**^{40}Ar*/^{39}Ar**	**Age (yrs)**	**Age error (yrs)**	**% error**	**^{39}Ar/^{40}Ar**	**^{39}Ar/^{40}Ar error**	**^{36}Ar/^{40}Ar**	**^{36}Ar/^{40}Ar error**
3.8	1	2.39733E-01	9.81222E-02	5.06609E+01	4.72635E+01	8.46390E-01	1.85566E-01	5.5	0.6	0.03	27.1	1.02109E+02	1.91206E+08	6.96963E+07	36.450884	2.88518E-03	3.14784E-04	2.44199E-03	4.68402E-04
4	1	1.40582E-01	2.78589E-02	-1.03582E+00	-1.30130E+01	5.73175E-01	5.47049E-02	19.7	0.8	0.13	59.3	2.49496E+02	4.35732E+08	2.61638E+07	6.0045595	2.38002E-03	9.49966E-05	1.36417E-03	1.20154E-04
4.2	1	2.87866E-02	1.14985E-02	1.07274E+01	5.66075E+00	1.12323E-01	2.06232E-02	46.9	1.0	0.37	69.0	7.61497E+01	1.44483E+08	4.57620E+06	3.1672837	9.25226E-03	2.09686E-04	1.03924E-03	1.89595E-04
4.4	1	3.48386E-02	4.97656E-03	-2.27057E-01	-2.43264E+00	7.87158E-02	9.21253E-03	112.8	2.6	0.96	68.9	5.21158E+01	1.00120E+08	3.57783E+06	3.5735489	1.32412E-02	3.31033E-04	1.04229E-03	1.20063E-04
4.5	1	7.41918E-02	1.50206E-02	-7.24885E+00	-7.25789E+00	2.35665E-01	2.51200E-02	39.1	0.8	1.16	48.1	6.45962E+01	1.23293E+08	7.28508E+06	5.9087449	7.37263E-03	2.14365E-04	1.73747E-03	1.84625E-04
4.6	1	3.48604E-02	1.23430E-02	-3.00269E+00	-5.85542E+00	1.00886E-01	1.99447E-02	46.9	1.6	1.40	61.4	4.76868E+01	9.18239E+07	6.34070E+06	6.9052778	1.28169E-02	5.53155E-04	1.29304E-03	2.54107E-04
4.7	1	1.46564E-02	6.21171E-03	-2.35479E-01	-3.68826E+00	-5.32916E-03	-1.28721E-02	77.6	2.0	1.81	102.8	5.77210E+01	1.10564E+08	3.33276E+06	3.0143217	1.78353E-02	5.59640E-04	-9.50470E-05	-2.29570E-04
4.8	1	1.98155E-03	7.29202E-03	-5.03769E+00	-3.94547E+00	1.47137E-04	1.43593E-02	70.1	2.1	2.17	99.9	4.56575E+01	8.80100E+07	4.59260E+06	5.2182666	2.16475E-02	1.13923E-03	3.18517E-06	3.10843E-04
4.9	1	7.92995E-03	7.61380E-03	9.33876E+00	4.21018E+00	6.65670E-03	1.48745E-02	68.2	1.8	2.52	96.1	5.00874E+01	9.63251E+07	3.38846E+06	3.5177372	1.96395E-02	6.83534E-04	1.30734E-04	2.92119E-04
5	1	1.11027E-02	5.58952E-03	6.57172E+00	3.32854E+00	3.51791E-02	1.16254E-02	86.2	2.1	2.97	83.9	5.56316E+01	1.06678E+08	3.42450E+06	3.2101321	1.53264E-02	4.22869E-04	5.39169E-04	1.77863E-04
5.1	1	1.06902E-02	3.28243E-03	5.21107E+00	1.74913E+00	8.08416E-03	6.17140E-03	158.4	3.1	3.79	95.6	5.31633E+01	1.02076E+08	2.44655E+06	2.3967932	1.82223E-02	4.21086E-04	1.47312E-04	1.12435E-04
5.2	1	1.16185E-02	2.09619E-03	5.46828E+00	1.07467E+00	5.73097E-03	3.71666E-03	269.0	6.4	5.18	96.8	5.33300E+01	1.02387E+08	2.55349E+06	2.4939504	1.84120E-02	4.49672E-04	1.05519E-04	6.83883E-05
5.3	1	1.25514E-02	1.29348E-03	5.60243E+00	7.15199E-01	3.95244E-03	2.41459E-03	420.0	7.2	7.36	98.0	5.89235E+01	1.12797E+08	2.04917E+06	1.8166899	1.68551E-02	2.97110E-04	6.66190E-05	4.06834E-05
5.4	1	2.15094E-02	9.02316E-04	3.29885E+00	3.42619E-01	3.86764E-02	1.51098E-03	788.9	10.9	11.45	84.9	6.54787E+01	1.24921E+08	2.10103E+06	1.6818908	1.30743E-02	1.83303E-04	5.05667E-04	1.84946E-05
5.5	1	1.84744E-02	5.25736E-04	2.88950E+00	8.38726E-02	8.78294E-03	3.17454E-04	3872.8	34.8	31.52	96.0	6.38101E+01	1.21842E+08	1.29766E+06	1.0650336	1.51595E-02	1.37536E-04	1.33145E-04	4.66375E-06
5.55	1	1.70608E-02	3.89193E-04	2.77360E+00	8.63176E-02	4.86531E-03	1.69185E-04	7513.2	61.4	70.47	97.6	5.86041E+01	1.12204E+08	1.10824E+06	0.9876976	1.67715E-02	1.38486E-04	8.15983E-05	2.75948E-06
5.575	1	1.49278E-02	1.22671E-03	2.69954E+00	5.59931E-01	3.17141E-03	1.99491E-03	497.3	9.3	73.04	98.4	5.88048E+01	1.12577E+08	2.20530E+06	1.9589311	1.68551E-02	3.22627E-04	5.34545E-05	3.36100E-05
5.65	1	1.51448E-02	1.25700E-03	5.15597E+00	6.01928E-01	1.36084E-02	2.17209E-03	484.3	8.8	75.56	93.4	5.83788E+01	1.11786E+08	2.22382E+06	1.9893559	1.62025E-02	3.00389E-04	2.20491E-04	3.49707E-05
fuse	1	1.68410E-02	4.75756E-04	2.84282E+00	1.16472E-01	6.28642E-03	2.53363E-04	4716.1	40.0	100.00	97.0	6.02387E+01	1.15236E+08	1.17030E+06	1.0155726	1.62156E-02	1.38676E-04	1.01938E-04	4.01771E-06

Sample #	Phase	J factor	J abs err	Batch Number															
79	Hbl	1.09061E-03	7.22766E-06	UVM005															
Watts	**Time (min)**	**^{38}Ar/^{39}Ar**	**^{38}Ar/^{39}Ar error**	**^{37}Ar/^{39}Ar**	**^{37}Ar/^{39}Ar error**	**^{36}Ar/^{39}Ar**	**^{36}Ar/^{39}Ar error**	**^{39}Ar (cps)**	**^{39}Ar error**	**Cumul % ^{39}Ar**	**% ^{40}Ar***	**^{40}Ar*/^{39}Ar**	**Age (yrs)**	**Age error (yrs)**	**% error**	**^{39}Ar/^{40}Ar**	**^{39}Ar/^{40}Ar error**	**^{36}Ar/^{40}Ar**	**^{36}Ar/^{40}Ar error**
3.8	1	9.62190E-02	4.79177E-02	4.13486E+01	1.85529E+01	4.57869E-01	9.56078E-02	13.2	0.7	0.19	78.3	5.13332E+02	8.02069E+08	4.76884E+07	5.9456737	1.58402E-03	9.16881E-05	7.25273E-04	1.46187E-04
4.2	1	2.04010E-02	1.03978E-02	6.13473E+00	3.96683E+00	8.65940E-02	2.07842E-02	57.5	1.8	1.00	73.6	7.31287E+01	1.38434E+08	6.68157E+06	4.8265251	1.02013E-02	3.76042E-04	8.83371E-04	2.10880E-04
4.4	1	1.45185E-02	2.56269E-02	1.65841E+01	9.32547E+00	7.65559E-02	4.81689E-02	24.5	0.7	1.34	54.1	2.86847E+01	5.55737E+07	9.01924E+06	16.229333	2.00819E-02	1.88041E-03	1.53739E-03	9.75864E-04
4.6	1	1.93367E-02	9.47713E-03	1.06211E+01	3.58446E+00	4.58063E-02	2.00419E-02	63.8	1.9	2.25	80.8	5.87802E+01	1.12097E+08	5.15659E+06	4.6001162	1.40724E-02	5.42032E-04	6.44603E-04	2.81804E-04
4.8	1	2.18944E-02	3.27892E-03	9.38433E+00	1.14396E+00	2.32609E-02	6.15417E-03	203.5	4.8	5.13	89.4	5.96366E+01	1.13680E+08	3.14878E+06	2.7698674	1.53045E-02	3.85246E-04	3.55995E-04	9.38648E-05
4.9	1	2.31394E-02	2.77082E-03	5.53407E+00	9.45705E-01	1.62860E-02	5.23105E-03	229.7	6.2	8.37	92.0	5.66470E+01	1.08148E+08	3.28219E+06	3.0348968	1.64594E-02	4.66417E-04	2.68058E-04	8.58269E-05
5	1	1.86769E-02	2.49730E-03	6.25982E+00	8.62410E-01	2.79418E-02	4.27936E-03	269.1	5.5	12.18	88.7	6.66130E+01	1.26522E+08	3.02997E+06	2.394815	1.35043E-02	2.88578E-04	3.77334E-04	5.73112E-05
5.1	1	1.99183E-02	1.13435E-03	3.61482E+00	3.25884E-01	1.96545E-02	1.67962E-03	715.2	10.4	22.29	92.0	6.77419E+01	1.28592E+08	2.15441E+06	1.6753879	1.36914E-02	2.02890E-04	2.69099E-04	2.26730E-05
5.2	1	1.83836E-02	6.91687E-04	3.26093E+00	2.16435E-01	1.06162E-02	9.53754E-04	1188.1	15.8	39.09	95.1	6.15699E+01	1.17248E+08	1.76354E+06	1.5041146	1.55664E-02	2.08814E-04	1.65256E-04	1.46878E-05
5.3	1	1.84889E-02	7.94453E-04	2.18733E+00	2.29820E-01	1.08797E-02	1.14748E-03	1037.0	12.6	53.76	94.9	6.07676E+01	1.15768E+08	1.63288E+06	1.4104788	1.57105E-02	1.93872E-04	1.70926E-04	1.79097E-05
5.4	1	1.16821E-02	3.81600E-03	1.17749E+01	1.58082E+00	2.43743E-02	6.59029E-03	162.5	4.7	56.06	89.1	6.09204E+01	1.16050E+08	3.82172E+06	3.2931726	1.50030E-02	4.52932E-04	3.65689E-04	9.83527E-05
fuse	1	2.09650E-02	6.84565E-04	3.49369E+00	9.77059E-02	9.86342E-03	4.28042E-04	3107.2	29.8	100.00	95.3	6.06915E+01	1.15628E+08	1.35322E+06	1.17033	1.58445E-02	1.53308E-04	1.56281E-04	6.61806E-06

Sample #	Phase	J factor	J abs err	Batch Number															
22 (15AB22D)	Psd 1	1.08318E-03	5.74086E-06	UVM005															
Watts	**Time (min)**	**^{38}Ar/^{39}Ar**	**^{38}Ar/^{39}Ar error**	**^{37}Ar/^{39}Ar**	**^{37}Ar/^{39}Ar error**	**^{36}Ar/^{39}Ar**	**^{36}Ar/^{39}Ar error**	**^{39}Ar (cps)**	**^{39}Ar error**	**Cumul % ^{39}Ar**	**% ^{40}Ar***	**^{40}Ar*/^{39}Ar**	**Age (yrs)**	**Age error (yrs)**	**% error**	**^{39}Ar/^{40}Ar**	**^{39}Ar/^{40}Ar error**	**^{36}Ar/^{40}Ar**	**^{36}Ar/^{40}Ar error**
3.8	1	1.36582E-02	3.09949E-04	2.00937E-01	9.83193E-03	5.17153E-03	1.25400E-04	25657.0	197.5	9.12	62.0	2.53300E+00	4.94306E+06	6.85071E+04	1.39	2.46168E-01	1.94037E-03	1.27307E-03	2.93507E-05
3.9	1	1.27993E-02	3.27103E-04	1.54887E-01	9.49688E-03	6.03037E-04	4.41965E-05	27328.2	207.8	18.82	94.2	2.95839E+00	5.77189E+06	5.74270E+04	0.99	3.19585E-01	2.49187E-03	1.92722E-04	1.40522E-05
4.1	1	1.17109E-02	2.58455E-04	1.85790E-01	9.25448E-03	9.34124E-04	4.39678E-05	28280.8	215.1	28.87	92.7	3.54794E+00	6.91990E+06	6.91490E+04	1.00	2.62217E-01	2.03973E-03	2.44943E-04	1.13846E-05
4.3	1	1.33502E-02	4.30188E-04	4.22402E-01	1.49282E-02	1.92189E-03	6.65807E-05	20043.3	155.0	35.99	85.9	3.52798E+00	6.88103E+06	7.38047E+04	1.07	2.45802E-01	1.96574E-03	4.72404E-04	1.59818E-05
4.6	1	1.23261E-02	3.28113E-04	2.63089E-01	9.31975E-03	9.71105E-04	4.51480E-05	28036.1	213.1	45.95	93.0	3.86742E+00	7.54172E+06	7.57213E+04	1.00	2.41718E-01	1.90726E-03	2.34734E-04	1.07777E-05
4.9	1	1.16429E-02	2.34299E-04	1.97416E-01	9.74994E-03	1.19983E-03	4.76158E-05	28101.5	212.8	55.94	91.7	3.96020E+00	7.72224E+06	7.72597E+04	1.00	2.32378E-01	1.79726E-03	2.78815E-04	1.08705E-05
5.2	1	1.17733E-02	2.96532E-04	2.12233E-01	1.13109E-02	1.71687E-03	9.75762E-05	25016.5	193.7	64.82	88.4	3.93756E+00	7.67820E+06	8.03887E+04	1.05	2.25550E-01	1.79316E-03	3.87240E-04	2.18142E-05
5.5	1	1.23883E-02	2.86631E-04	1.73683E-01	7.54120E-03	1.70252E-03	4.25762E-05	37926.5	290.0	78.30	88.6	3.96558E+00	7.73272E+06	7.97284E+04	1.03	2.24189E-01	1.74732E-03	3.81686E-04	9.10610E-06
5.8	1	1.28117E-02	3.31885E-04	1.79389E-01	9.26966E-03	2.57422E-03	9.47191E-05	27512.5	207.9	88.07	83.2	3.81282E+00	7.43545E+06	8.00207E+04	1.08	2.18944E-01	1.69705E-03	5.63611E-04	2.03198E-05
6.1	1	1.25019E-02	3.20385E-04	2.06985E-01	2.79767E-02	2.99016E-03	1.34038E-04	8955.8	76.5	91.25	80.9	3.78914E+00	7.38936E+06	9.26690E+04	1.25	2.14344E-01	1.96685E-03	6.40924E-04	2.82846E-05
fuse	1	1.40524E-02	3.40361E-04	1.83608E-01	1.14443E-02	9.38503E-03	2.72544E-04	24617.6	188.8	100.00	57.0	3.72875E+00	7.27183E+06	1.06930E+05	1.47	1.53538E-01	1.20057E-03	1.44095E-03	4.04209E-05

Sample #	Phase	J factor	J abs err	Batch Number															
22 (15AB22D)	Psd 2	1.08318E-03	5.74086E-06	UVM005															
Watts	**Time (min)**	**^{38}Ar/^{39}Ar**	**^{38}Ar/^{39}Ar error**	**^{37}Ar/^{39}Ar**	**^{37}Ar/^{39}Ar error**	**^{36}Ar/^{39}Ar**	**^{36}Ar/^{39}Ar error**	**^{39}Ar (cps)**	**^{39}Ar error**	**Cumul % ^{39}Ar**	**% ^{40}Ar***	**^{40}Ar*/^{39}Ar**	**Age (yrs)**	**Age error (yrs)**	**% error**	**^{39}Ar/^{40}Ar**	**^{39}Ar/^{40}Ar error**	**^{36}Ar/^{40}Ar**	**^{36}Ar/^{40}Ar error**
3.8	1	1.42636E-02	4.44962E-04	1.15499E-01	2.54699E-02	9.15002E-03	2.78079E-04	23849.5	423.5	6.51	45.9	2.33058E+00	4.54856E+06	1.77825E+05	3.91	1.97960E-01	3.52896E-03	1.81134E-03	4.47636E-05
3.9	1	1.25385E-02	3.73670E-04	1.10896E-01	1.50635E-02	1.28783E-03	6.82073E-05	38156.0	675.1	16.93	88.3	2.89607E+00	5.65048E+06	1.17993E+05	2.09	3.05474E-01	5.43551E-03	3.93400E-04	1.96523E-05
4	1	1.23893E-02	3.86328E-04	1.11756E-01	2.10786E-02	1.15967E-03	9.63794E-05	27048.0	480.3	24.32	89.8	3.04526E+00	5.94109E+06	1.22522E+05	2.06	2.95489E-01	5.27905E-03	3.42669E-04	2.78296E-05
4.1	1	1.22503E-02	4.32586E-04	1.37513E-01	2.35915E-02	1.30026E-03	9.71171E-05	25037.4	444.7	31.15	89.8	3.43611E+00	6.70220E+06	1.37753E+05	2.06	2.62192E-01	4.67767E-03	3.40919E-04	2.47399E-05
4.2	1	1.19558E-02	3.64833E-04	1.85929E-01	4.23864E-02	1.80328E-03	1.03711E-04	13422.1	239.9	34.82	87.2	3.66874E+00	7.15503E+06	1.53280E+05	2.14	2.38553E-01	4.32421E-03	4.30176E-04	2.35523E-05
4.4	1	1.38299E-02	4.60375E-04	4.66843E-01	3.75130E-02	9.86438E-03	3.44824E-04	15512.4	276.2	39.06	53.0	3.36738E+00	6.56838E+06	2.21949E+05	3.38	1.59499E-01	2.85469E-03	1.57336E-03	4.74137E-05
4.7	1	1.40155E-02	4.51784E-04	2.41397E-01	2.33641E-02	1.11869E-02	4.29856E-04	23650.6	419.8	45.51	53.1	3.80594E+00	7.42207E+06	2.50696E+05	3.38	1.40447E-01	2.50228E-03	1.57116E-03	5.36004E-05
5.1	1	1.45095E-02	4.38252E-04	2.68720E-01	1.81425E-02	1.55835E-02	4.63985E-04	32846.3	582.2	54.48	46.2	4.02738E+00	7.85297E+06	3.02612E+05	3.85	1.15623E-01	2.05402E-03	1.80182E-03	4.31585E-05
5.4	1	1.25809E-02	3.87745E-04	2.60690E-01	2.00672E-02	6.55539E-03	2.59085E-04	30228.1	536.3	62.74	67.6	4.10643E+00	8.00677E+06	2.14087E+05	2.67	1.65609E-01	2.94892E-03	1.08563E-03	3.83773E-05
5.7	1	1.25968E-02	3.82781E-04	2.12264E-01	1.54835E-02	5.23043E-03	2.21509E-04	36774.7	651.3	72.78	71.7	3.96927E+00	7.73989E+06	1.95412E+05	2.52	1.81464E-01	3.22262E-03	9.49133E-04	3.65328E-05
6	1	1.26671E-02	3.88507E-04	1.89185E-01	1.50332E-02	4.69320E-03	1.55120E-04	35973.3	636.8	82.60	73.6	3.91869E+00	7.64147E+06	1.88110E+05	2.46	1.88603E-01	3.34663E-03	8.85152E-04	2.47311E-05
6.3	1	1.22988E-02	4.74776E-04	3.68465E-02	3.08965E-02	4.34354E-03	2.00635E-04	17318.3	308.0	87.33	74.7	3.82880E+00	7.46655E+06	1.83227E+05	2.45	1.95273E-01	3.49357E-03	8.48176E-04	3.61958E-05
fuse	1	1.30286E-02	3.65685E-04	1.68932E-01	2.12238E-02	6.96989E-03	2.39766E-04	46398.3	820.6	100.00	64.9	3.87151E+00	7.54967E+06	2.09182E+05	2.77	1.68489E-01	2.98582E-03	1.17435E-03	3.46761E-05

Sample #	Phase	J factor	J abs err	Batch Number
23 (15AB23)	Psd 1	1.08921E-03	4.90144E-06	UVM005

Watts	Time (min)	^{38}Ar/^{39}Ar	^{38}Ar/^{39}Ar error	^{37}Ar/^{39}Ar	^{37}Ar/^{39}Ar error	^{36}Ar/^{39}Ar	^{36}Ar/^{39}Ar error	^{39}Ar (cps)	^{39}Ar error	Cumul % ^{39}Ar	% ^{40}Ar*	^{40}Ar*/^{39}Ar	Age (yrs)	Age error (yrs)	% error	^{39}Ar/^{40}Ar	^{39}Ar/^{40}Ar error	^{36}Ar/^{40}Ar	^{36}Ar/^{40}Ar error
3.8	1	1.34540E-02	2.75680E-04	1.89323E-01	2.25883E-02	5.31552E-03	1.28637E-04	11880.0	95.6	7.52	62.6	2.67573E+00	5.25021E+06	7.43417E+04	1.42	2.35373E-01	1.96940E-03	1.25113E-03	2.87017E-05
4	1	1.22101E-02	2.72505E-04	1.53350E-01	9.11438E-03	5.38438E-04	4.12944E-05	28830.6	218.7	25.76	94.8	2.96970E+00	5.82609E+06	5.50309E+04	0.94	3.20390E-01	2.47804E-03	1.72510E-04	1.31680E-05
4.2	1	1.15194E-02	2.24313E-04	1.05127E-01	1.58454E-02	6.78353E-04	6.78134E-05	17487.9	136.0	36.82	94.8	3.68181E+00	7.22034E+06	6.95715E+04	0.96	2.57881E-01	2.06150E-03	1.74935E-04	1.74379E-05
4.5	1	1.30357E-02	4.23664E-04	5.31186E-01	4.14851E-02	1.41722E-03	1.14937E-04	10495.1	86.0	43.46	89.5	3.66563E+00	7.18867E+06	7.63789E+04	1.06	2.47150E-01	2.13439E-03	3.50267E-04	2.82778E-05
5	1	1.24703E-02	3.79988E-04	2.16653E-01	1.57621E-02	8.23357E-04	7.06537E-05	17162.0	133.1	54.32	94.3	4.09270E+00	8.02434E+06	7.73100E+04	0.96	2.31387E-01	1.85014E-03	1.90514E-04	1.62858E-05
5.5	1	1.12486E-02	2.36961E-04	2.92383E-01	1.34537E-02	1.36333E-03	5.76204E-05	21471.5	166.2	67.90	91.0	4.15474E+00	8.14572E+06	8.02312E+04	0.98	2.20350E-01	1.75321E-03	3.00409E-04	1.24941E-05
6	1	1.20063E-02	2.74900E-04	1.70709E-01	9.12906E-03	1.79260E-03	4.79052E-05	28432.5	219.1	85.89	88.2	4.01358E+00	7.86957E+06	7.87542E+04	1.00	2.20483E-01	1.72925E-03	3.95236E-04	1.01303E-05
6.5	1	1.22148E-02	3.32803E-04	1.66173E-01	4.04147E-02	2.38627E-03	1.59125E-04	6515.7	57.1	90.01	84.5	3.89063E+00	7.62900E+06	9.21634E+04	1.21	2.17860E-01	2.05834E-03	5.19873E-04	3.44155E-05
fuse	1	1.28836E-02	3.51186E-04	2.44836E-01	2.57986E-02	5.41629E-03	1.73248E-04	15783.7	123.9	100.00	69.9	3.77348E+00	7.39975E+06	9.11146E+04	1.23	1.86231E-01	1.49086E-03	1.00868E-03	3.13173E-05

Sample #	Phase	J factor	J abs err	Batch Number
23 (15AB23)	Psd 2	1.08921E-03	4.90144E-06	UVM005

Watts	Time (min)	^{38}Ar/^{39}Ar	^{38}Ar/^{39}Ar error	^{37}Ar/^{39}Ar	^{37}Ar/^{39}Ar error	^{36}Ar/^{39}Ar	^{36}Ar/^{39}Ar error	^{39}Ar (cps)	^{39}Ar error	Cumul % ^{39}Ar	% ^{40}Ar*	^{40}Ar*/^{39}Ar	Age (yrs)	Age error (yrs)	% error	^{39}Ar/^{40}Ar	^{39}Ar/^{40}Ar error	^{36}Ar/^{40}Ar	^{36}Ar/^{40}Ar error
3.8	1	1.53104E-02	5.97184E-04	3.67163E-01	3.02329E-02	1.21468E-02	5.61726E-04	20005.3	355.9	5.89	36.0	2.07239E+00	4.06769E+06	2.00101E+05	4.92	1.76498E-01	3.15463E-03	2.14389E-03	9.15919E-05
3.9	1	1.34884E-02	4.28159E-04	2.98230E-01	2.14534E-02	1.94442E-03	9.50396E-05	28658.9	508.3	14.32	81.9	2.65340E+00	5.20646E+06	1.15521E+05	2.22	3.11391E-01	5.56372E-03	6.05475E-04	2.76077E-05
4.05	1	1.21168E-02	3.83805E-04	1.25666E-01	1.79819E-02	1.00149E-03	4.86152E-05	32545.5	577.9	23.90	91.5	3.22910E+00	6.33409E+06	1.26781E+05	2.00	2.84151E-01	5.06718E-03	2.84575E-04	1.28653E-05
4.2	1	1.24181E-02	4.21637E-04	2.78489E-01	2.68586E-02	1.67562E-03	9.87885E-05	24007.4	427.1	30.96	86.6	3.26128E+00	6.39711E+06	1.34839E+05	2.11	2.67418E-01	4.78721E-03	4.48091E-04	2.52025E-05
4.4	1	1.33004E-02	5.04278E-04	5.71142E-01	3.69146E-02	4.71853E-03	1.90539E-04	18323.7	327.2	36.36	70.6	3.42856E+00	6.72462E+06	1.71756E+05	2.55	2.08831E-01	3.75097E-03	9.85378E-04	3.57407E-05
4.7	1	1.45340E-02	6.15393E-04	8.17828E-01	3.97577E-02	6.04283E-03	2.21156E-04	17646.0	314.9	41.55	66.3	3.61513E+00	7.08984E+06	1.91407E+05	2.70	1.86965E-01	3.35748E-03	1.12980E-03	3.61700E-05
5.1	1	1.21927E-02	3.76361E-04	4.35294E-01	2.64701E-02	2.28320E-03	1.05047E-04	28697.4	508.3	49.99	85.0	3.90354E+00	7.65425E+06	1.62633E+05	2.12	2.19869E-01	3.91085E-03	5.02005E-04	2.13316E-05
5.5	1	1.15126E-02	3.51174E-04	3.23234E-01	1.84054E-02	1.80651E-03	8.31512E-05	39028.8	690.3	61.48	88.3	4.08228E+00	8.00396E+06	1.64271E+05	2.05	2.17681E-01	3.86681E-03	3.93243E-04	1.67237E-05
5.8	1	1.20332E-02	3.72962E-04	1.83249E-01	2.12340E-02	2.02768E-03	9.58645E-05	31106.8	552.2	70.63	86.7	3.97132E+00	7.78687E+06	1.63346E+05	2.10	2.19259E-01	3.90493E-03	4.44588E-04	1.94912E-05
6.2	1	1.18455E-02	3.84496E-04	2.79770E-01	2.35809E-02	2.26281E-03	7.50883E-05	26687.1	474.1	78.49	85.3	3.94293E+00	7.73134E+06	1.64734E+05	2.13	2.17654E-01	3.88328E-03	4.92509E-04	1.38273E-05
fuse	1	1.27612E-02	3.45124E-04	3.46415E-01	1.73616E-02	5.19518E-03	1.75013E-04	73108.3	1291.4	100.00	71.0	3.83228E+00	7.51481E+06	1.89065E+05	2.52	1.86841E-01	3.30664E-03	9.70673E-04	2.78636E-05

Sample #	Phase	J factor	J abs err	Batch Number
3A (5MT3A)	Psd 1	5.38491E-04	1.83087E-06	UVM007

Watts	Time (min)	^{38}Ar/^{39}Ar	^{38}Ar/^{39}Ar error	^{37}Ar/^{39}Ar	^{37}Ar/^{39}Ar error	^{36}Ar/^{39}Ar	^{36}Ar/^{39}Ar error	^{39}Ar (cps)	^{39}Ar error	Cumul % ^{39}Ar	% ^{40}Ar*	^{40}Ar*/^{39}Ar	Age (yrs)	Age error (yrs)	% error	^{39}Ar/^{40}Ar	^{39}Ar/^{40}Ar error	^{36}Ar/^{40}Ar	^{36}Ar/^{40}Ar error
3.8	1	6.15470E-02	6.06069E-03	7.77658E-01	8.48219E-02	1.93348E-01	2.97435E-02	92.7	2.2	1.12	48.4	5.43700E+01	5.28135E+07	2.85954E+06	5.41	8.93297E-03	2.37590E-04	1.72717E-03	2.63428E-04
4	1	2.21631E-02	9.48805E-04	6.17256E-01	2.01628E-02	4.48719E-02	3.79769E-03	881.0	12.9	11.79	41.3	9.49775E+00	9.33641E+06	3.61841E+05	3.88	4.38021E-02	7.04599E-04	1.96549E-03	1.64393E-04
4.3	1	1.82021E-02	9.12747E-04	3.02521E-01	1.11003E-02	2.08653E-02	1.80994E-03	1647.2	16.2	31.74	52.8	6.99150E+00	6.87736E+06	1.53211E+05	2.23	7.58207E-02	8.85877E-04	1.58202E-03	1.36700E-04
4.6	1	1.44287E-02	3.58407E-04	3.84202E-01	9.03284E-03	1.81955E-02	1.32505E-03	2505.3	21.0	62.09	56.6	7.13713E+00	7.02034E+06	1.21861E+05	1.74	7.98021E-02	7.74555E-04	1.45204E-03	1.05273E-04
4.9	1	1.80759E-02	8.70768E-04	1.41134E+00	3.21346E-02	2.16871E-02	2.03837E-03	1502.2	15.9	80.29	54.6	7.90970E+00	7.77865E+06	1.75100E+05	2.25	7.01363E-02	8.66300E-04	1.52105E-03	1.42381E-04
5.3	1	1.64866E-02	7.26031E-04	8.28471E-01	2.06564E-02	3.17773E-02	3.00192E-03	994.8	12.1	92.33	53.4	1.09497E+01	1.07595E+07	2.80164E+05	2.60	4.91285E-02	6.83506E-04	1.56117E-03	1.46623E-04
6	1	3.37668E-02	2.59182E-03	2.91577E+00	1.00467E-01	1.21900E-01	1.38587E-02	235.6	5.0	95.19	38.5	2.30520E+01	2.25785E+07	1.31022E+06	5.80	1.69097E-02	3.83203E-04	2.06130E-03	2.30846E-04
8	1	8.44643E-02	6.44395E-03	8.96208E+00	3.53180E-01	3.91823E-01	3.02516E-02	112.0	3.8	96.54	33.2	5.92680E+01	5.74973E+07	5.81252E+06	10.11	5.71175E-03	1.97100E-04	2.23799E-03	1.56122E-04
fuse	1	7.90542E-02	5.05590E-03	5.16393E+00	1.32292E-01	2.62977E-01	1.35476E-02	285.3	5.6	100.00	41.2	5.56089E+01	5.39994E+07	2.58984E+06	4.80	7.49384E-03	1.50995E-04	1.97070E-03	9.41019E-05

Sample #	Phase	J factor	J abs err	Batch Number
3A (5MT3A)	Psd 2	5.38491E-04	1.83087E-06	UVM007

Watts	Time (min)	^{38}Ar/^{39}Ar	^{38}Ar/^{39}Ar error	^{37}Ar/^{39}Ar	^{37}Ar/^{39}Ar error	^{36}Ar/^{39}Ar	^{36}Ar/^{39}Ar error	^{39}Ar (cps)	^{39}Ar error	Cumul % ^{39}Ar	% ^{40}Ar*	^{40}Ar*/^{39}Ar	Age (yrs)	Age error (yrs)	% error	^{39}Ar/^{40}Ar	^{39}Ar/^{40}Ar error	^{36}Ar/^{40}Ar	^{36}Ar/^{40}Ar error
3.8	1	1.48905E-01	6.42667E-03	1.72391E+00	4.36693E-01	7.49418E-01	3.21792E-02	284.8	7.9	1.10	31.6	1.03951E+02	9.96817E+07	8.52058E+06	8.55	3.05877E-03	8.51189E-05	2.29229E-03	7.54763E-05
3.9	1	5.20858E-02	2.18381E-03	1.55263E+00	1.57146E-01	1.91078E-01	5.31742E-03	833.4	12.6	4.32	34.6	3.04312E+01	2.97477E+07	1.31751E+06	4.43	1.14693E-02	1.77752E-04	2.19154E-03	5.16292E-05
4	1	2.86819E-02	1.14087E-03	7.23238E-01	8.02042E-02	8.70105E-02	4.85754E-03	1551.0	17.4	10.30	22.1	7.47500E+00	7.35201E+06	3.90077E+05	5.31	2.99934E-02	3.56012E-04	2.60974E-03	1.43056E-04
4.2	1	2.52459E-02	7.09155E-04	7.51409E-01	4.86920E-02	6.19806E-02	2.07156E-03	2808.7	22.5	21.15	41.6	1.33150E+01	1.30755E+07	2.72709E+05	2.09	3.15409E-02	2.73001E-04	1.95493E-03	6.37543E-05
4.4	1	1.80704E-02	5.05472E-04	5.92322E-01	2.90642E-02	2.75000E-02	7.23407E-04	4733.4	33.7	39.42	49.5	8.10931E+00	7.97453E+06	1.26577E+05	1.59	6.15582E-02	4.76582E-04	1.69285E-03	4.31789E-05
4.6	1	1.64989E-02	4.55961E-04	8.31757E-01	2.67809E-02	2.16795E-02	9.50621E-04	5210.3	32.6	59.54	52.3	7.19119E+00	7.07341E+06	9.44884E+04	1.34	7.36739E-02	5.04177E-04	1.59722E-03	6.94633E-05
4.8	1	1.84186E-02	4.62608E-04	1.79812E+00	6.56191E-02	2.55956E-02	8.16633E-04	3871.7	28.3	74.48	49.6	7.70943E+00	7.58211E+06	1.21097E+05	1.60	6.58921E-02	5.22006E-04	1.68655E-03	5.26278E-05
5.1	1	2.08240E-02	6.67963E-04	1.05677E+00	4.74634E-02	4.04679E-02	1.12102E-03	2795.4	23.4	85.28	46.7	1.07098E+01	1.05245E+07	1.99505E+05	1.90	4.41194E-02	3.89031E-04	1.78542E-03	4.74252E-05
5.6	1	3.64365E-02	1.32099E-03	2.89546E+00	1.78287E-01	1.00786E-01	2.58478E-03	1405.4	12.6	90.70	44.5	2.44696E+01	2.39579E+07	4.97856E+05	2.08	1.84507E-02	1.71309E-04	1.85958E-03	4.49268E-05
6.3	1	6.79974E-02	3.08848E-03	6.32006E+00	2.52592E-01	2.51672E-01	7.27632E-03	574.2	7.7	92.92	39.9	5.08219E+01	4.94131E+07	1.65758E+06	3.35	7.99719E-03	1.09304E-04	2.01267E-03	5.19244E-05
7.5	1	7.50529E-02	2.12322E-03	4.63386E+00	1.42768E-01	3.07133E-01	1.01227E-02	1037.5	11.9	96.92	43.0	6.98894E+01	6.76133E+07	1.80473E+06	2.67	6.22099E-03	7.26112E-05	1.91067E-03	5.91200E-05
fuse	1	1.28344E-01	4.68807E-03	6.29972E+00	3.34122E-01	5.66945E-01	2.02977E-02	796.5	11.6	100.00	42.0	1.23914E+02	1.18219E+08	4.01728E+06	3.40	3.42833E-03	5.05650E-05	1.94367E-03	6.36903E-05

Batch Number	Flux Monitor	Flux Monitor Age Reference	Decay Constants	Atmospheric Ar Ratios	Mass Discrimination	±	(^{40}Ar/^{39}Ar)$_K$	±	(^{36}Ar/^{37}Ar)$_{Ca}$	±	(^{39}Ar/^{37}Ar)$_{Ca}$	±	Correction Factor References
UVM005	Fish Canyon Tuff Sanidine	Renne et al. (1993)	Steiger and Jäger (1977)	Lee et al. (2006)	304.7	2.3	8.869E-03	5.298E-03	2.728E-04	1.833E-05	6.750E-04	1.728E-05	Measured at UVM
UVM007	Fish Canyon Tuff Sanidine	Kuiper et al. (2008)	Min et al. (2000)	Lee et al. (2006)	307.4	1.5	5.400E-04	1.400E-04	2.650E-04	2.200E-05	6.950E-04	8.966E-02	Jicha & Brown (2014); Renne et al. (2013)